

On the Relation between the Mysterious $21\ \mu\text{m}$ Emission Feature of Post-Asymptotic Giant Branch Stars and Their Mass Loss Rates

DRAFT: 2018.10.17.452

Ajay Mishra¹, Aigen Li¹, and B.W. Jiang²

ABSTRACT

Over two decades ago, a prominent, mysterious emission band peaking at $\sim 20.1\ \mu\text{m}$ was serendipitously detected in four preplanetary nebulae (PPNe; also known as “protoplanetary nebulae”). To date, this spectral feature, designated as the “ $21\ \mu\text{m}$ ” feature, has been seen in 27 carbon-rich PPNe in the Milky Way and the Magellanic Clouds. The nature of its carriers remains unknown although many candidate materials have been proposed. The $21\ \mu\text{m}$ sources also exhibit an equally mysterious, unidentified emission feature peaking at $30\ \mu\text{m}$. While the $21\ \mu\text{m}$ feature is *exclusively* seen in PPNe, a short-lived evolutionary stage between the end of the asymptotic giant branch (AGB) and planetary nebula (PN) phases, the $30\ \mu\text{m}$ feature is more commonly observed in all stages of stellar evolution from the AGB through PPN to PN phases. We derive the stellar mass loss rates (\dot{M}) of these sources from their infrared (IR) emission, using the “2-DUST” radiative transfer code for axisymmetric dusty systems which allows one to distinguish the mass loss rates of the AGB phase (\dot{M}_{AGB}) from that of the superwind (\dot{M}_{SW}) phase. We examine the correlation between \dot{M}_{AGB} or \dot{M}_{SW} and the fluxes emitted from the 21 and $30\ \mu\text{m}$ features. We find that both features tend to correlate with \dot{M}_{AGB} , suggesting that their carriers are probably formed in the AGB phase. The nondetection of the $21\ \mu\text{m}$ feature in AGB stars suggests that, unlike the $30\ \mu\text{m}$ feature, the excitation of the carriers of the $21\ \mu\text{m}$ feature may require ultraviolet photons which are available in PPNe but not in AGB stars.

¹Department of Physics and Astronomy, University of Missouri, Columbia, MO 65211, USA; amishra@mail.missouri.edu, lia@missouri.edu

²Department of Astronomy, Beijing Normal University, Beijing 100875, China; bjiang@bnu.edu.cn

Subject headings: circumstellar matter — dust, extinction — infrared: stars — stars: AGB and Post-AGB — stars: evolution

1. Introduction

Historically, the evolutionary stage of low- to intermediate-mass stars ($\sim 0.8\text{--}8 M_{\odot}$) in between the end of the asymptotic giant branch (AGB) phase and the planetary nebula (PN) phase has been designated as the proto-planetary nebula phase. This short evolutionary phase of $\sim 10^3$ yr is now also called “preplanetary nebula” (e.g., see Sahai et al. 2005) because the phrase “proto-planetary” is widely used by the exoplanetary and planet formation communities to refer to dusty disks around young stars. Following Sahai et al. (2005), in this work we will use the term “preplanetary nebula” (PPN). We also note that, in the literature, the term preplanetary (or proto-planetary) nebulae (PPNe) has been interchangeably used with the term post-AGB objects.

The so-called “ $21 \mu\text{m}$ ” PPNe, a class of C-rich PPNe which all exhibit a prominent emission feature at $21 \mu\text{m}$, have received increasing attention over the past decades. This feature was serendipitously discovered by Kwok et al. (1989) in four PPNe through the $7.7\text{--}22.6 \mu\text{m}$ spectra obtained by the *Low Resolution Spectrometer* (LRS) on board the *Infrared Astronomical Satellite* (IRAS). So far, this feature has been seen unambiguously in 27 carbon-rich PPNe, including 18 Galactic objects (Cerrigone et al. 2011) and nine objects in the Large and Small Magellanic Clouds (Volk et al. 2011). The spectral profile of the so-called “ $21 \mu\text{m}$ ” feature displays little variation among different sources: it always peaks at $\sim 20.1 \mu\text{m}$ and has a more or less constant FWHM (full width at half maximum) of $\sim 2.2\text{--}2.3 \mu\text{m}$.

The exact nature of the carriers of this feature remains unknown ever since its discovery in 1989. This feature is potentially an important probe of the physical and chemical processes occurring in PPNe, a short evolutionary stage immediately preceding the PN phase. Also, it is important in terms of energetics since this feature emits up to $\sim 8\%$ of the total infrared (IR) power of a $21 \mu\text{m}$ source. The fact that so much power is carried in this feature suggests that its carrier must be made of abundant elements (e.g., C). Over the past decades, over a dozen carrier candidates have been suggested (e.g., see Posch et al. 2004, Zhang et al. 2009a). However, none of them can be considered viable because they either could not reproduce the observed spectral profile (e.g., SiC [see Jiang et al. 2005], FeO [see Li et al. 2013]) or they require too much dust material (e.g., TiC [see Li 2003]).

A unique characteristics of the mysterious $21 \mu\text{m}$ feature is that it is so far only detected

in PPNe, neither in the AGB phase nor in the PN phase. This might suggest that the condensation of the carriers of the $21\ \mu\text{m}$ feature may occur during the so-called superwind phase (e.g., see von Helden et al. 2000), a phase of high mass-loss where AGB stars lose the remaining stellar envelope and terminate their life on the AGB (see Renzini 1981). It is also possible that, after entering the PN phase, the $21\ \mu\text{m}$ -feature carriers may be rapidly destroyed by the highly energetic photons available in PNe. To examine this hypothesis, in this work we derive the stellar mass loss rates of the $21\ \mu\text{m}$ PPNe during the AGB phase as well as the superwind phase and explore the correlation between the $21\ \mu\text{m}$ feature and the mass loss rates, with an aim of gaining insight into the formation and destruction of the carriers of this mysterious feature.

2. The $21\ \mu\text{m}$ Sources: Photometry and Spectroscopy

We will derive the mass loss rates of the $21\ \mu\text{m}$ sources from their infrared (IR) emission spectral energy distributions (SEDs). In this work we will consider all the 18 Galactic $21\ \mu\text{m}$ sources. The IR emission of these sources have been measured with various instruments through broadband photometry: (i) the *Infrared Astronomical Satellite* (IRAS) at 12, 25, 60, and $100\ \mu\text{m}$, (ii) the *Midcourse Space Experiment* (MSX) *A*, *C*, *D*, and *E* bands respectively at 8.28, 12.13, 14.65 and $21.3\ \mu\text{m}$, (iii) the *Infrared Camera* (IRC) on board the AKARI satellite at 9 and $18\ \mu\text{m}$, and (iv) the *Wide-field Infrared Survey Explorer* (WISE) at 3.4, 4.6, 12 and $22\ \mu\text{m}$. Six of these 18 sources have also been measured at 1.2 mm with the *Max-Planck Millimeter Bolometer* (MAMBO) array at the 30-meter IRAM telescope (Buemi et al. 2007). We compile from the literature the stellar and circumstellar parameters of all the 18 Galactic $21\ \mu\text{m}$ sources and tabulate them in Table 1. These include the stellar effective temperature T_{eff} , stellar luminosity L_{\star} , stellar core mass M_{\star} , stellar radius r_{\star} , and distance d from Earth of the central star. Also tabulated in Table 1 are the *IRAS*, *MSX*, *AKARI*, *WISE* and *IRAM/MAMBO* photometry.

In addition to the $21\ \mu\text{m}$ feature, the $21\ \mu\text{m}$ sources also display a prominent, mysterious emission feature at $30\ \mu\text{m}$. The $30\ \mu\text{m}$ feature is very broad and strong and extends from $\sim 24\ \mu\text{m}$ to $\sim 45\ \mu\text{m}$. It often accounts for up to $\sim 30\%$ of the total IR luminosity of such an object (Volk et al. 2002).

The $21\ \mu\text{m}$ sources also exhibit a distinctive set of emission features at 3.3, 6.2, 7.7, 8.6, and $11.3\ \mu\text{m}$ (Hrivnak et al. 2008, Volk 2015). These features are collectively known as the “unidentified infrared” (UIR) features and commonly attributed to polycyclic aromatic hydrocarbon (PAH) molecules (Léger & Puget 1984, Allamandola et al. 1985).

For these sources, high-quality mid-IR spectra have been obtained with the *Infrared Spectrograph* (IRS) on board the *Spitzer Space Telescope* and the *Short Wavelength Spectrometer* (SWS) on board the *Infrared Space Observatories* (ISO). These spectra allow one to measure relatively accurately the (integrated) fluxes emitted in the $21\ \mu\text{m}$ feature (F_{21}) and the $30\ \mu\text{m}$ feature (F_{30}), and to a lesser degree, the UIR features (F_{UIR}).¹

Mishra, Li & Jiang (2015) had used the PAHFIT software of Smith et al. (2007) to decompose the *Spitzer*/IRS or *ISO*/SWS spectra of ten Galactic $21\ \mu\text{m}$ sources and had already determined F_{21} , F_{30} , and F_{UIR} for these ten sources. Following Mishra, Li & Jiang (2015), we analyze the *Spitzer*/IRS or *ISO*/SWS spectra of the remaining eight sources and decompose their IR spectra into (i) a stellar continuum $B_\lambda(T_{\text{eff}})$ which is approximated by a blackbody at the stellar effective temperature T_{eff} , (ii) a thermal continuum of warm dust of temperature T_W represented by a modified blackbody $\lambda^{-2} B_\lambda(T_W)$, (iii) a thermal continuum of cold dust of temperature T_C represented by $\lambda^{-2} B_\lambda(T_C)$, and (iv) the $21\ \mu\text{m}$, $30\ \mu\text{m}$ and UIR features approximated by a set of Drude functions. In addition, the H_2 S(0)–S(7) rotational lines are included and approximated by a number of Gaussian fits. In Figure 1 we show the spectral decomposition fits to the eight sources. In Table 2 we tabulate the fluxes emitted in the $21\ \mu\text{m}$, $30\ \mu\text{m}$ and UIR features.

3. Stellar Mass Loss Rates

We employ the “2-DUST” radiative transfer code to model the dust IR emission of the selected $21\ \mu\text{m}$ sources, using the *IRAS* (and the $1.2\ \text{mm}$ IRAM/MAMBO, if available) photometric data. The “2-DUST” code, developed by Ueta & Meixner (2003) for dusty axisymmetric systems, is well suited for modeling the IR emission of the PPN layered dust shells.

Following Ueta & Meixner (2003), we consider a dust density function that has (i) a spherical outer shell – the remnant of the AGB wind, (ii) a spheroidal mid-region, and (iii) an inner toroidal core created during the superwind phase – a rather brief period of equatorially-enhanced mass-loss near the end of the AGB mass-loss phase. The mid-region of the shell assumes a somewhat spheroidal distribution, reflecting the transition from a spherical mass-loss geometry to an axial symmetry during the course of the AGB mass-loss history. The underlying assumption of this axisymmetric density distribution function is that the mass loss in the AGB phase is spherically symmetric and converted to axisymmetric after

¹For some sources the *Spitzer*/IRS or *ISO*/SWS data are available only at $\lambda \gtrsim 10\ \mu\text{m}$. Therefore, for these sources F_{UIR} is underestimated as the UIR bands at 6.2 , 7.7 and $8.6\ \mu\text{m}$ are not counted in F_{UIR} .

the end of the AGB phase (i.e., the “superwind” phase). The adopted density distribution is a function of the radius of the dust shell r , the latitudinal angle Θ , and five geometric parameters (A , B , C , D , and E ; see Meixner et al. 2002, Ueta & Meixner 2003):

$$\rho(r, \Theta) = \rho_{\min} \left(\frac{r}{r_{\min}} \right)^{-B} \left\{ 1 + C \sin^F \Theta \left[e^{-(r/r_{\text{sw}})^D} / e^{-(r_{\min}/r_{\text{sw}})^D} \right] \right\} \times \left\{ 1 + A (1 - \cos \Theta)^F \left[e^{-(r/r_{\text{sw}})^E} / e^{-(r_{\min}/r_{\text{sw}})^E} \right] \right\}, \quad (1)$$

where $\rho(r, \Theta)$ is the dust mass density at radius r and latitude Θ , ρ_{\min} is the dust mass density on the polar axis at the inner edge of the shell, r_{\min} is the inner radius of the shell, r_{\max} is the outer radius of the shell, r_{sw} is the radius of the superwind between r_{\min} and the AGB wind which defines the “thickness” of the inner, axisymmetric region of the shell. The model parameters r_{\min} , r_{sw} and r_{\max} , when available, are taken from the literature where these parameters are constrained by the optical and IR morphology (see Table 3). The expansion velocity v_{exp} is also taken from the literature, which was mostly determined from the CO line emission.

This function defines a three-layer density distribution. The outermost region has a spherically-symmetric, power-law density distribution $\rho(r, \Theta) \propto r^{-B}$ which results from the early AGB mass loss occurring in an almost perfect spherical symmetry. The density distribution of the inner-most region is axisymmetric and has an equatorial enhancement. The equatorial enhancement is considered to be caused by the axisymmetric superwind at the end of the AGB phase. The degree of the equatorial enhancement is controlled by A (with $A = 0$ corresponding to spherical symmetry, i.e., no enhancement). The equatorial enhancement can be made disk-like or toroidal-like by the “flatness” parameter F , with small F values for toroidal density distributions and large F values for disk-like structures. The transitional mid-region is controlled by C , the shell elongation parameter. It turns on and off the latitudinal dependence of the radial fall-off parameter, B . The D and E parameters describe the “abruptness” of the geometrical transition: the larger D and E are, the more abrupt is the dissipation of the latitudinal variation in the density distribution (see Ueta & Meixner 2003).

For the dust composition, we only consider amorphous carbon dust. The $21 \mu\text{m}$ and $30 \mu\text{m}$ carriers are not included in our modeling for three reasons: (1) their carriers are unidentified; (2) their excitation mechanisms are unknown, i.e., are they nano-sized and undergo transient heating by single stellar photons [Draine & 2001, Liu et al. 2002] like FeO [Li et al. 2013] and TiC nanoparticles [Li 2003] or sub- μm -sized and attain an equilibrium temperature like SiC [Jiang et al. 2005] and hydrogenated amorphous carbon [HAC; Zhang et

al. 2009a])? and (3) we are mainly interested to derive the dust mass loss rates. The carriers of the $21\ \mu\text{m}$ and $30\ \mu\text{m}$ features are not important as far as the mass loss rates are concerned (see Hony et al. 2002, 2003, Hony & Bouwman 2004). The absorption and scattering cross sections are computed with Mie theory, using the dielectric functions of amorphous carbon of Rouleau & Martin (1991).

For the dust size distribution, we take a MRN-type power-law distribution function of $dn/da \propto a^{-\beta}$ for $a_{\min} < a < a_{\max}$, where a is the spherical radius of the dust (we assume the dust to be spherical) with a lower and upper cutoff of $a_{\min} = 50\ \text{\AA}$ and $a_{\max} = 0.25\ \mu\text{m}$, respectively (see Mathis et al. 1977). For a given dust size distribution and a given dust shell structure, the optical depth τ_{λ} at wavelength λ is directly related to the dust quantity.

Admittedly, the 2-DUST model involves many parameters (see Ueta & Meixner 2003). General considerations help explore parameter space. The equatorial enhancement parameter A which sets the equator-to-pole density ratio ($\rho_{\text{eq}}/\rho_{\text{pol}} = 1 + A$) is mainly constrained by the mid-IR emission from warm dust (i.e., the *IRAS* $25\ \mu\text{m}$ photometry of the $21\ \mu\text{m}$ sources). Generally speaking, models with high A values produce more mid-IR emission. The radial-falloff parameter B is strongly tied to the mass-loss dynamics: $B = 2$ for a steady mass loss, $B > 2$ for a steadily increasing mass loss, and $B < 2$ for a diminishing mass loss (see Ueta & Meixner 2003). The B parameter is mainly constrained by the cold dust emission at $\lambda \gtrsim 100\ \mu\text{m}$, particularly by the $1.2\ \text{mm}$ emission. For models with a larger B value, more dust will be concentrated radially closer to the central star and a larger amount of warmer dust will be present in the shell and will therefore emit too much at the mid-IR and too little in the far-IR at $\lambda \gtrsim 100\ \mu\text{m}$. In view that for 12 over 18 of our sources there is no $1.2\ \text{mm}$ photometry available and the longest wavelength data available so far is the *IRAS* $100\ \mu\text{m}$ photometry. It is therefore possible that our SED modeling may favor large B values. To avoid this, we intend to choose the smallest B value which still fits the observed SED. The shell elongation parameter C only slightly affects the far-IR emission: models with a larger C produces slightly more emission at $\lambda > 100\ \mu\text{m}$. Model SEDs with different D , E , and F parameters also show very little difference in the IR. The model parameters (particularly C , D , E and F) would be better constrained by the optical and IR morphology of the $21\ \mu\text{m}$ sources (see Ueta & Meixner 2003).

The 21 and $30\ \mu\text{m}$ features could appreciably contribute to the mid-IR broadband photometry. Particularly, an appreciable fraction of the $21.34\ \mu\text{m}$ *MSX* E -band flux of each source could arise from the $21\ \mu\text{m}$ feature. This is probably also true for the *AKARI* $18\ \mu\text{m}$ band, the *WISE* $22\ \mu\text{m}$ band, and the *IRAS* $25\ \mu\text{m}$ band. The broad $30\ \mu\text{m}$ feature could account for a smaller (but not necessarily negligible) fraction of these broadband detections. Since the carriers of the 21 and $30\ \mu\text{m}$ features are not included in our model, the contri-

butions of these features to the broadband photometry need to be subtracted. To this end, we approximate the 21 and 30 μm features of each source by four Drude profiles respectively peaking at 20.1, 26, 30, and 33 μm and integrate the sum of these Drude profiles with the filter functions of the *AKARI* 18 μm band, the 21.34 μm *MSX E* band, the *WISE* 22 μm band, and the *IRAS* 25 μm band. In Table 4 we tabulate the contributions of the 21 and 30 μm features of each source to the photometric fluxes of these bands. In the following, unless otherwise stated, the mid-IR photometric fluxes refer to the feature-subtracted broadband photometry. It is these feature-subtracted photometric fluxes that we will model.

The inclination (θ) of a nebula is best constrained by the observed nebula morphology. For some of our sources, the inclination angles have already been derived in the literature from their resolved optical and/or near-IR images. For these sources, we adopt the inclination angles reported in the literature (see Table 3). For the remaining sources, we consider 10 different inclination angles increasing from $\theta = 0^\circ$ (i.e., pole-on) to $\theta = 90^\circ$ (i.e., edge-on) at a step of $\Delta\theta = 10^\circ$. We take the inclination angle which provides the best fit to the observed SED.

Figure 2 shows the model fits to the observed dust and stellar photometry of the six Galactic sources for which the 1.2 mm flux has been measured by IRAM/MAMBO. The overall fits are reasonably satisfactory. We note that we do not intend to fit the *ISO/Spitzer* spectroscopy as we are mostly interested to derive the dust mass loss rates. The *Spitzer/IRS* or *ISO/SWS* spectra overlaid in the SED fit mostly serve as a guide. For IRAS 20000+3239, the model could not fit the IRAS 100 μm flux. In view of the overall SED, it is likely that the IRAS 100 μm flux could have been overestimated.

Figures 3 and 4 show the model fits to the observed SEDs of the 12 Galactic sources for which there are no reported 1.2 mm IRAM/MAMBO measurements. Similarly, the model fits the observational data fairly well, although it fails at reproducing the 21 μm and 30 μm emission features as it is not our intention to fit these features. Similar to IRAS 20000+3239, for IRAS 05113+1347, IRAS 05341+0852, IRAS 13245-5036, IRAS 19477+2401, and IRAS 23304+6147, the IRAS 100 μm flux could have been overestimated. In order to examine whether the lack of any photometric data at $\lambda > 100 \mu\text{m}$ would “miss” the dust that is cold and located in the outer region of the shell (leading to an underestimate of the dust mass), we also fit the SEDs of the six sources shown in Figure 2 for which the 1.2 mm photometric data are available, but neglecting the 1.2 mm photometry. We find that the dust mass derived from ignoring the 1.2 mm data only differs by $< 30\%$ from that in which the 1.2 mm data are included. This is because, except for IRAS 20000+3239, the 60, 100 μm and 1.2 mm data do not deviate much from a single power-law and thus no cold component is missing.

In Table 3 we list the model parameters for the dust density function (A , B , C , D , E ,

and F), the dust size distribution power index β , the expansion velocity v_{exp} , and the inner (r_{min}) and outer (r_{max}) boundaries of the PPN dust shell. It is seen from Table 3 that the best-fit models for all the Galactic $21\ \mu\text{m}$ sources favor $B > 2$, implying a non-steady mass-loss process. As illustrated in eq. 1, the B factor also couples with the density distribution of the SW component. Therefore, our best-fit models suggest that both the AGB mass-loss and the SW mass-loss are not constant (i.e., $B \neq 2$). While in the literature a steady mass-loss is often assumed for modeling the millimeter data of CO and even for the dust IR emission SED modeling, we note that a constant mass-loss rate is often an idealistic and simplified assumption. The production of the mass loss is a complicated process involving both the pulsation of the surface layers of AGB stars and the stellar radiation pressure on dust (see Habing et al. 1994). Near the end of the AGB phase, one expects an accelerating increase in mass loss (see Renzini 1981, Gail & Sedlmayr 2014). Therefore, one would not expect a constant mass-loss rate along the AGB evolution. Nevertheless, if there is only limited observational information about the CO emission or the dust IR emission, it is not unreasonable to adopt $B = 2$.

With the assumption of constant velocity mass loss, we calculate the time scale (τ) for each source by dividing the size of the extended dust shell with its expansion velocity v_{exp} . For the AGB phase, we obtain a time scale of $\tau_{\text{AGB}} = (r_{\text{max}} - r_{\text{sw}})/v_{\text{exp}}$. For the superwind phase, the time scale is $\tau_{\text{sw}} = (r_{\text{sw}} - r_{\text{min}})/v_{\text{exp}}$ (see Ueta & Meixner 2003). Our model calculations indicate that the short duration of the intense mass loss from most of the post-AGB stars in the AGB phase to be $\sim 10^3$ years and the superwind phase to be $\sim 10^2$ years. The dust mass for most of the sources in the AGB and superwind phases is in the range of $\sim 10^{-3} M_{\odot}$. The average mass loss rate for each phase (\dot{M}_{AGB} , \dot{M}_{sw}) is calculated from the dust mass ($M_{\text{dust}}^{\text{AGB}}$, $M_{\text{dust}}^{\text{sw}}$) and the duration of mass loss (τ_{AGB} , τ_{sw}) assuming a gas-to-dust mass ratio of ~ 280 appropriate for C-rich AGB stars (Justtanont et al. 1996), i.e., $\dot{M}_{\text{AGB}} = 280 M_{\text{dust}}^{\text{AGB}}/\tau_{\text{AGB}}$ and $\dot{M}_{\text{sw}} = 280 M_{\text{dust}}^{\text{sw}}/\tau_{\text{sw}}$. In Table 7 we tabulate the dust masses and mass loss rates of each source in the AGB and superwind phases. Due to the inter-dependencies of the model parameters, we estimate the uncertainties from the range of parameters used in our model calculations. We note that the actual dust masses and mass-loss rates are expected to be somewhat larger since the carriers of the 21 and $30\ \mu\text{m}$ features are not included in our SED fitting. The carriers of these features, particularly that of the $30\ \mu\text{m}$ feature, are expected to account for an appreciable fraction of the total dust mass since they account for a substantial fraction of the total IR luminosity. However, without knowing the mineralogical compositions and optical properties of their carriers, we are not able to determine their masses.

To gauge the range over which a parameter could vary while the overall model fit to the observed SED remains acceptable, following the approach of Sargent et al. (2010), we

allow the dust IR fluxes to deviate by one to three times the uncertainties, as estimated by eye, while keeping all other parameters at their best-fit values. Figure 5 demonstrates this estimation of uncertainty by eye for the optical depth parameter $\tau_{9.8}$ at wavelength $\lambda = 9.8 \mu\text{m}$ for IRAS 07134+1005, given as dashed curves calculated from models with $\tau_{9.8}$ set to the extremes of its allowable range. The uncertainties on the other parameters are determined in a similar way for all 18 sources.

Finally, we admit that, to accurately explore parameter space, the SED modeling itself is not sufficient. A simultaneous modeling of the SEDs and the resolved scattered-light images in the optical/near-IR as well as other data (e.g., spectropolarimetry) would allow many parameters to be more accurately explored (e.g., see Oppenheimer et al. 2005). Nevertheless, the parameters derived here are generally consistent with that from more sophisticated models. For example, for the common source IRAS 04296+3429, our mass loss rate and mass loss duration agree with that of Oppenheimer et al. (2005) within the uncertainty range.

4. Results and Discussion

We now explore the relation of the $21 \mu\text{m}$ feature with the stellar mass loss rates. We take the flux emitted from the $21 \mu\text{m}$ feature F_{21} of ten $21 \mu\text{m}$ sources determined by Mishra, Li & Jiang (2015) and that of eight sources derived in §2 (see Table 2 and Figure 2). To cancel the distance effect, we multiply the mass loss rates by $(d/1 \text{ kpc})^{-2}$, where d is the distance of the source to Earth.

In Figure 6 we plot the flux emitted from the $21 \mu\text{m}$ feature (F_{21}) against the stellar mass loss rates \dot{M} of the AGB phase (\dot{M}_{AGB}) and the PPN superwind phase (\dot{M}_{SW}), multiplied by $(d/1 \text{ kpc})^{-2}$. A linear parametric test leads to a Pearson correlation coefficient of $R \approx 0.82$ for all the 18 Galactic sources. The correlation is significant at a $\sim 2.1\sigma$ level. We also perform a Kendall non-parametric test to measure the strength of dependence between F_{21} and \dot{M}_{AGB} or \dot{M}_{SW} . We derive a Kendall correlation coefficient of $\tau \approx 0.59$ and a corresponding probability $p \approx 6.46 \times 10^{-4}$ of a chance correlation at a 3σ significant level. Therefore, the $21 \mu\text{m}$ feature shows a tendency of correlating with \dot{M}_{AGB} . In contrast, with a Pearson correlation coefficient of $R \approx 0.59$ and a Kendall $\tau \approx 0.41$ and $p \approx 0.018$, the $21 \mu\text{m}$ feature shows a much weaker correlation with \dot{M}_{SW} , if at all. This suggests that the carriers of the $21 \mu\text{m}$ feature are probably formed in the AGB phase.

The nondetection of the $21 \mu\text{m}$ feature in AGB stars suggests that the excitation of its carriers may require ultraviolet (UV) photons which are available in PPNs but not in AGB stars. More likely, the $21 \mu\text{m}$ feature carriers could be embedded in or attached to some sort

of bulk carbon dust (e.g., sub- μm -sized HAC) as nano-sized “islands” or “side-groups units”. Upon leaving the AGB phase, the UV photons of PPNe break them away from the bulk dust and excite them to emit at $21\ \mu\text{m}$. Ultimately, they are destroyed by the much harder UV photons in PNe. This explains the exclusive detection of the $21\ \mu\text{m}$ feature in PPNe.

The $21\ \mu\text{m}$ sources also emit strongly at the $30\ \mu\text{m}$ feature (Volk 2015). While the $21\ \mu\text{m}$ feature is only detected in PPNe, the $30\ \mu\text{m}$ feature is more commonly seen in carbon-rich objects at various evolutionary stages, spanning the AGB, PPN and PN phases (see Jiang et al. 2010, Zhang & Jiang 2008). First detected in several carbon stars and in two PNe (Forrest et al. 1981), the $30\ \mu\text{m}$ feature also remains unidentified. Magnesium sulfide (MgS) dust, the most popular candidate carrier (Goebel & Moseley 1985, Nuth et al. 1985, Jiang et al. 1999, Szczerba et al. 1999, Hony et al. 2002, 2003, Lombaert et al. 2012), has recently been ruled out as a valid carrier since it would require too much S to account for the observed fluxes of the $30\ \mu\text{m}$ feature (see Zhang et al. 2009b; also see Messenger et al. 2013, Otsuka et al. 2014).

We have also examined the correlation of the $30\ \mu\text{m}$ feature with the stellar mass loss rates \dot{M}_{AGB} and \dot{M}_{SW} . As shown in Figure 7, with a Pearson correlation coefficient of $R \approx 0.81$ and a Kendall $\tau \approx 0.71$ and $p \approx 1.24 \times 10^{-5}$, the $30\ \mu\text{m}$ feature shows a moderate correlation with \dot{M}_{AGB} . This, consistent with its detection in AGB stars, implies that its carriers condense in the AGB phase and its excitation does not require UV photons. Figure 7 also shows that, with $R \approx 0.77$, $\tau \approx 0.58$ and $p \approx 8.51 \times 10^{-4}$, the $30\ \mu\text{m}$ feature and the superwind is somewhat correlated, suggesting that the $30\ \mu\text{m}$ feature carriers could also condense in the superwind.

Based on the principal component analysis (PCA) method, we have also applied a fully non-parametric multivariate analysis to the four variables F_{21} , F_{30} , \dot{M}_{AGB} and \dot{M}_{SW} to determine their possible correlations and statistical significance. As shown in Table 6, the results derived from the PCA multivariate analysis technique are in close agreement with that of the Pearson linear parametric analysis and that of the Kendall non-parametric analysis: while the $21\ \mu\text{m}$ feature appears to correlate with \dot{M}_{AGB} but not with \dot{M}_{SW} , the $30\ \mu\text{m}$ feature seems to correlate with both \dot{M}_{AGB} and \dot{M}_{SW} .

In Figure 8 we show the correlations of F_{21} and F_{30} with the total IR emission $F_{\text{IR}} \equiv \int F_{\lambda} d\lambda$ obtained by integrating the observed dust IR SED over the entire wavelength range. While it is apparent that both F_{21} and F_{30} correlate with F_{IR} , the latter shows a closer correlation with F_{IR} than the former. This supports the idea of the condensation of the $21\ \mu\text{m}$ feature carrier mainly occurring in the AGB phase while the $30\ \mu\text{m}$ feature carrier could condense both in the AGB phase and in the superwind phase. If one assumes that all kinds of dust species are proportionally condensed, one would expect F_{21} to be proportional

to the IR power $F_{\text{IR}}^{\text{AGB}}$ emitted by the bulk dust generated in the AGB phase. In contrast, F_{30} is expected to be proportional to the total IR power $F_{\text{IR}} = F_{\text{IR}}^{\text{AGB}} + F_{\text{IR}}^{\text{SW}}$ emitted both by the bulk dust generated in the AGB phase ($F_{\text{IR}}^{\text{AGB}}$) and by the bulk dust generated in the superwind ($F_{\text{IR}}^{\text{SW}}$). It is worth noting that while the mass loss rates \dot{M}_{AGB} and \dot{M}_{SW} derived in §3 have not included the (unknown) carriers of the 21 and 30 μm features, the total IR emission F_{IR} is obtained by integrating over the entire SED and therefore does include the contributions from both features. The fact that the correlations of F_{IR} with F_{21} and F_{30} are consistent with the correlations of \dot{M}_{AGB} (and \dot{M}_{SW} for the 30 μm feature as well) with F_{21} and F_{30} implies that the exclusion of the 21 and 30 μm feature carriers in deriving the mass loss rates does not affect our correlation studies.

The 21 μm sources also emit at the UIR bands (Hrivnak et al. 2008). However, the spectral profiles of the UIR bands of the Galactic 21 μm sources are “unusual” in the sense that they appear substantially different from that of the typical interstellar UIR bands (see Peeters et al. 2002). Most notably, while at $\sim 8 \mu\text{m}$ the interstellar UIR bands have two well-separated features at 7.7 and 8.6 μm , the Galactic 21 μm sources have a broad 8 μm feature. The UIR features are widely seen in PPNe, PNe and the interstellar medium (ISM). However, they are rarely seen in AGB stars. The few C stars that display the UIR features all have a hot companion that emits UV photons (Speck & Barlow 1997, Boersma et al. 2006). In the context of PAHs as the carriers of the UIR features, one may ascribe the nondetection of the UIR features in C stars to that, due to lack of UV photons in cool C-rich AGB stars, PAHs, even present in the circumstellar envelopes around C-rich AGB stars, may not be sufficiently excited to emit in the near- and mid-IR. However, Li & Draine (2002) have demonstrated that the excitation of PAHs does not require UV photons, and the visible/near-IR photons available in C stars are capable of exciting PAHs to emit at the “UIR” bands. The visible/near-IR absorption spectra measured by Mattioda et al. (2005) for PAH ions further support the finding of Li & Draine (2002) that PAHs can be excited by the soft stellar photons from C stars.

In principle, it would be of great value to examine the correlation of the UIR features with the stellar mass loss rates \dot{M}_{AGB} and \dot{M}_{SW} . *If* the UIR features are shown to correlate with \dot{M}_{AGB} , one could speculate that their carriers, like that of the 21 μm feature, could form in the AGB phase as aromatic “islands” embedded in bulk HAC dust. The nondetection of the UIR bands in AGB stars could merely indicate that the carriers of the UIR features could not be knocked off the bulk dust by the photons of AGB stars as free-flying aromatic hydrocarbon molecules. Unfortunately, the *Spitzer*/IRS or *ISO*/SWS spectra of the 21 μm sources do not always span all the UIR bands. More specifically, for some sources there lack spectroscopic data at $\lambda < 10 \mu\text{m}$ (e.g., see Figure 1) which prevents an accurate determination of F_{UIR} . Therefore, we do not intend to explore the possible correlation between F_{UIR}

and \dot{M}_{AGB} or \dot{M}_{SW} .

Finally, we note that we have not considered the nine $21\ \mu\text{m}$ sources detected in the Large Magellanic Cloud (LMC) and the Small Magellanic Cloud (SMC) both of which are metal-poor: the metallicity of the LMC is $\sim 1/4$ of that in the Galaxy (Russell & Dopita 1992), while the metallicity of the SMC is only $\sim 1/10$ of that of the Galaxy (Kurt & Dufour 1998). With respect to the overall mid-IR emission and the UIR emission, the relative strengths of the 21 and $30\ \mu\text{m}$ features of the Magellanic Cloud sources are appreciably weaker than that of the Galactic $21\ \mu\text{m}$ sources. Also, the spectral appearance of the UIR features of the Magellanic Cloud $21\ \mu\text{m}$ sources is remarkably different from that of the Galaxy. While most of the Galactic $21\ \mu\text{m}$ sources have “unusual” UIR spectral profiles, the Magellanic Cloud $21\ \mu\text{m}$ sources show more “normal” looking UIR features. Therefore, we prefer not to investigate the relation between F_{UIR} and \dot{M}_{AGB} or \dot{M}_{SW} of the Galactic and Magellanic Cloud $21\ \mu\text{m}$ sources as one class. The UIR carriers of the Galactic $21\ \mu\text{m}$ sources could be richer in aliphatics than that of the ISM and the Magellanic Cloud $21\ \mu\text{m}$ sources (see Li & Draine 2012, Yang et al. 2013).

5. Summary

We have modeled the dust IR emission SEDs of the $21\ \mu\text{m}$ sources using the 2-DUST radiative transfer code for axisymmetric dusty systems. We have derived their mass loss rates in the AGB and superwind phases. We have explored the correlation between the mass loss rates and the unidentified $21\ \mu\text{m}$ and $30\ \mu\text{m}$ features seen in carbon-rich PPNe. The principal results of this paper are the following:

1. The $21\ \mu\text{m}$ feature which is only seen in carbon-rich PPNe tends to correlate with \dot{M}_{AGB} but not with \dot{M}_{SW} , suggesting that its carrier could condense in the AGB phase but its excitation and/or generation requires UV photons which are available in PPNe but not in AGB stars. The $21\ \mu\text{m}$ feature carrier could be destroyed by the more energetic photons available in PNe.
2. The $30\ \mu\text{m}$ feature which is seen in AGB stars, PPNe and PNe correlates with \dot{M}_{AGB} and, to a less degree, with \dot{M}_{SW} , suggesting that its carrier could condense both in the AGB phase and in the superwind and it can be excited by visible/near-IR photons.

Acknowledgements

We thank Archana Mishra, Angela Speck, Ke Zhang and the anonymous referee for their valuable comments and discussions. We are supported in part by NSF AST-1311804, NNX13AE63G, NSFC 11273022, NSFC 11473023, and the University of Missouri Research Board.

REFERENCES

- Allamandola, L.J., Tielens, A.G.G.M., & Barker, J.R. 1985, *ApJL*, 290, L25
- Bakker, J.E., van Dishoeck, E.F., Waters, L.B.F.M., & Schoenmaker, T. 1997, *A&A*, 323, 469
- Boersma, C., Hony, S., & Tielens, A.G.G.M. 2006, *A&A*, 447, 213
- Bouwman, J., de Koter, A., van den Ancker, M.E., & Waters, L.B.F.M. 2000, *A&A*, 360, 213
- Buemi, C.S., Umana, G., Trigilio, C., & Leto, P. 2007, *A&A*, 462, 637
- Bujarrabal, V., Castro-Carrizo, A., Alcolea, J., & Sanchez Contreras, C. 2001, *A&A*, 377, 868
- Cerrigone, L., Hora, J. L., Umana, G., Trigilio, C., Hart, A., & Fazio, G. 2011, *ApJ*, 738, 121
- Clube, K. L., & Gledhill, T. M. 2004, *MNRAS*, 355, L17
- Draine, B. T., & Li, A. 2001, *ApJ*, 551, 807
- Forrest, W.J., Houck, J.R., & McCarthy, J.F. 1981, *ApJ*, 248, 195
- Gail, H.-P., & Sedlmayr, E. 2014, *Physics and Chemistry of Circumstellar Dust Shells* (Cambridge, UK: Cambridge Univ. Press)
- Gledhill, T.M., Chrysostomou, A., Hough, J.H., & Yates, J.A. 2001, *MNRAS*, 322, 321
- Gledhill, T.M. 2005, *MNRAS*, 356, 883
- Goebel, J.H., & Moseley, S.H. 1985, *ApJ*, 290, L35
- Habing, H. J., Tignon, J., & Tielens, A. G. G. M. 1994, *A&A*, 286, 523

- Hony, S., Waters, L.B.F.M., & Tielens, A.G.G.M. 2002, *A&A*, 390, 533
- Hony, S., Tielens, A.G.G.M., Waters, L.B.F.M., & de Koter, A. 2003, *A&A*, 402, 211
- Hony, S., & Bouwman, J. 2004, *A&A*, 413, 981
- Hrivnak, B.J., & Kwok, S. 1991, *ApJ*, 368, 564
- Hrivnak, B.J. 1995, *ApJ*, 438, 341
- Hrivnak, B.J., & Kwok, S. 1999, *ApJ*, 513, 869
- Hrivnak, B.J., Volk, K., & Kwok, S. 2000, *ApJ*, 535, 275
- Hrivnak, B.J., & Reddy, B.E. 2003, *ApJ*, 590, 1049
- Hrivnak, B.J., & Biegging, J.H. 2005, *ApJ*, 624, 331
- Hrivnak, B.J., Volk, K., Geballe, T. R., & Kwok, S. 2008, in *Organic Matter in Space (IAU Symp. 251)*, ed. S. Kwok & S.A. Sanford (Cambridge: Cambridge Univ. Press), 213
- Hrivnak, B. J., Volk, K., & Kwok, S. 2009, *ApJ*, 694, 1147
- Hrivnak, B. J., Lu, W., Bohlender, D., et al. 2011, *ApJ*, 734, 25
- Jiang, B. W., Szczerba, R., & Deguchi, S. 1999, *A&A*, 344, 918
- Jiang, B. W., Zhang, K., & Li, A. 2005, *ApJ*, 630, L77
- Jiang, B. W., Zhang, K., & Li, A. 2010, *Earth, Planets, & Space*, 62, 105
- Jura, M. 1986, *ApJ*, 303, 327
- Justtanont, K., Skinner, C.J., & Tielens, A.G.G.M. 1994, *ApJ*, 435, 852
- Justtanont, K., Skinner, C.J., Tielens, A.G.G.M., & Baas, F. 1996, *ApJ*, 456, 337
- Knapp, G.R., Young, K., Lee, E., & Jorissen, A. 1998, *ApJS*, 117, 209
- Knapp, G.R., Crosas, M., Young, K., & Ivezić, Z. 2000, *ApJ*, 534, 324
- Kurt, C.M., & Dufour, R.J. 1998, *RevMexAA Conf. Ser.*, 7, 202
- Kwok, S., Volk, K., & Hrivnak, B. J. 1989, *ApJ*, 345, L51
- Kwok, S., Volk, K., & Hrivnak, B. J. 2002, *ApJ*, 573, 720

- Léger, A., & Puget, J.L. 1984, *A&A*, 137, L5
- Leung, C.M. 1976, *JQSRT*, 16, 559
- Li, A. 2003, *ApJ*, 599, L45
- Li, A., & Draine, B.T. 2002, *ApJ*, 572, 232
- Li, A., & Draine, B. T. 2012, *ApJ*, 760, L35
- Li, A., Liu, J.M., & Jiang, B.W. 2013, *ApJ*, 777, 111
- Liu, J.M., Jiang, B.W., & Li, A. 2012, *Science in China: Physics, Mechanics and Astronomy*, 42, 877
- Likkell, L., Morris, M., Omont, A., & Forveille, T. 1987, *A&A*, 173, L11
- Likkell, L., Forveille, T., Omont, A., & Morris, M. 1991, *A&A*, 246, 153
- Lombärt, R., de Vries, B.L., de Koter, A., Decin, L., Min, M., Smolders, K., Mutschke, H., & Waters, L.B.F.M. 2012, *A&A*, 544, L18
- Loup, C., Forveille, T., Omont, A., & Nyman, L.A. 1990, *A&A*, 227, L29
- Mathis, J.S., Rumpel, W., & Nordsieck, K.H. 1977, *ApJ*, 217, 425
- Mattioda, A.L., Allamandola, L.J., & Hudgins, D.M. 2005, *ApJ*, 629, 1183
- Meixner, M., Skinner, C.J., Graham, J.R., Keto, E., Jernigan, J.G., & Arens, J.F. 1997, *ApJ*, 482, 897
- Meixner, M., Ueta, T., Dayal, A., Hora, J.L., Fazio, G., Hrivnak, B. J., Skinner, C. J., Hoffmann, W. F., & Deutsch, L. K. 1999, *ApJS*, 122, 221
- Meixner, M., Ueta, T., Bobrowsky, M., & Speck, A. 2002, *ApJ*, 571, 936
- Meixner, M., Zalucha, A., Ueta, T., Fong, D., & Justtanont, K. 2004, *ApJ*, 614, 371
- Messenger, S.J., Speck, A., & Volk, K. 2013, *ApJ*, 764, 142
- Mishra, A., Li, A., & Jiang, B.W. 2015, *ApJ*, 802, 39
- Nakashima, J., Koning, N., Kwok, S., & Zhang, Y. 2009, *ApJ*, 692, 402
- Nuth, J.A., Moseley, S.H., Silverberg, R.F., Goebel, J.H., & Moore, W.J. 1985, *ApJ*, 290, L41

- Omont, A., Loup, C., Forveille, T., Hekkert, P., Habing, H., & Sivagnanam, P. 1993, *A&A*, 267, 515
- Oppenheimer, B. D., Biegging, J. H., Schmidt, G. D., et al. 2005, *ApJ*, 624, 957
- Otsuka, M., Kemper, F., Cami, J., Peeters, E., & Bernard-Salas, J. 2014, *MNRAS*, 437, 2577
- Peeters, E., Hony, S., van Kerckhoven, C., et al. 2002, *A&A*, 390, 1089
- Posch, T., Mutschke, H., & Andersen, A.C. 2004, *ApJ*, 616, 1167
- Reddy, B.E., & Parthasarathy, M. 1996, *AJ*, 112, 2053
- Reimers, D. 1975, *Memoires of the Societe Royale des Sciences de Liege*, 8, 369
- Renzini, A. 1981, in *Physical Processes in Red Giants*, ed. I.A. Iben Jr. & A. Renzini (Dordrecht: Reidel), 431
- Rouleau, F., & Martin, P.G. 1991, *ApJ*, 377, 526
- Russell, S.C., & Dopita, M.A. 1992, *ApJ*, 384, 508
- Sahai, R. 1999, *ApJ*, 524, L125
- Sahai, R., Sánchez Contreras, C., & Morris, M. 2005, *ApJ*, 620, 948
- Sahai, R., Morris, M., Contreras, C.S., & Claussen, M. 2007, *ApJ*, 134, 2200
- Sargent, B. A., Srinivasan, S., Meixner, M., et al. 2010, *ApJ*, 716, 878
- Smith, J.D.T., et al. 2007, *ApJ*, 656, 770
- Speck A. K., & Barlow, M. J. 1997, *Ap&SS*, 251, 115
- Su, K.Y.L., Hrivnak, B.J., & Kwok, S. 2001, *ApJ*, 122, 1525
- Szczerba, R., Henning, Th., Volk, K., Kwok, S., & Cox, P. 1999, *A&A*, 345, L39
- Ueta, T., Meixner, M., & Bobrowsky, M. 2000, *ApJ*, 528, 861
- Ueta, T., Meixner, M., Hinz, P.M., et al. 2001, *A&A*, 557, 831
- Ueta, T., & Meixner, M. 2003, *ApJ*, 586, 1338
- Ueta, T., Murakawa, K., & Meixner, M. 2005, *AJ*, 129, 1625

- Volk, K. 2015, *Highlights of Astronomy*, 16, 701
- Volk, K., Kwok, S., Hrivnak, B.J., & Szczerba, R. 2002, *ApJ*, 567, 412
- Volk, K., Hrivnak, B.J., Matsuura, M., et al. 2011, *ApJ*, 735, 127
- von Helden, G., Tielens, A.G.G.M., van Heijnsbergen, D., et al. 2000, *Science*, 288, 313
- Yang, X. J., Glaser, R., Li, A., & Zhong, J. X. 2013, *ApJ*, 776, 110
- Zhang, K., & Jiang, B.W. 2008, *Science in China: Physics, Mechanics and Astronomy*, 51, 1187
- Zhang, K., Jiang, B.W., & Li, A. 2009a, *MNRAS*, 396, 1247
- Zhang, K., Jiang, B.W., & Li, A. 2009b, *ApJ*, 702, 680

A. Comments on Individual Sources

We comment on the individual sources, focusing on the mass loss rates \dot{M} reported in the literature. We will see in the following that the mass loss rate determinations are complicated by (i) the unknown gas-to-dust mass ratio $M_{\text{gas}}/M_{\text{dust}}$ if one derives \dot{M} from the dust emission modeling, and (ii) the unknown CO-to-H₂ number density ratio $n(\text{CO})/n(\text{H}_2)$ if one derives \dot{M} from the CO emission lines. Nevertheless, the mass loss rates derived in this work are generally consistent with that reported in the literature. To facilitate comparison between our mass loss rates with that reported in the literature, we correct for the distance and gas-to-dust mass ratio dependencies (i.e., $\dot{M} \propto d^2 M_{\text{gas}}/M_{\text{dust}}$). See Table 7 for a summary.

IRAS Z02229+6208: This is a cool, highly reddened post-AGB star. It has an elliptically extended nebula as revealed by the polarization map of Ueta et al. (2005). We derive a mass loss rate of $\dot{M} \approx 1.94 \times 10^{-5} M_{\odot} \text{yr}^{-1}$ in the AGB phase. Hrivnak et al. (2000) modeled the 2–45 μm ISO spectrum of this source using the DUSTCD radiative transfer code of Leung (1976). Assuming a gas-to-dust mass ratio of $M_{\text{gas}}/M_{\text{dust}} = 330$, they derived $\dot{M}/\{(v_{\text{exp}}/\text{km s}^{-1}) \times (d/\text{kpc})\} \approx 1.3 \times 10^{-6} M_{\odot} \text{yr}^{-1}$, corresponding to a mass loss rate of $\dot{M} \approx 3.59 \times 10^{-5} M_{\odot} \text{yr}^{-1}$ for $d = 2.2 \text{ kpc}$, $v_{\text{exp}} = 14.8 \text{ km s}^{-1}$, and $M_{\text{gas}}/M_{\text{dust}} = 280$ which are adopted in this work. Hrivnak & Bieging (2005) estimated $\dot{M} \approx 1.4 \times 10^{-4} M_{\odot} \text{yr}^{-1}$ from

the CO $J = 4 - 3$ and $J = 2 - 1$ emission lines observed with the *Heinrich Hertz Telescope* (HHT)² at $d = 2.2$ kpc.

IRAS 04296+3429: This source is in the advanced post-AGB evolution stage with a bipolar lobe structure (Sahai 1999). Using 2-DUST, we derive a mass loss rate of $\dot{M} \approx 3.84 \times 10^{-5} M_{\odot} \text{yr}^{-1}$ in the AGB phase. Bakker et al. (1997) obtained the optical high resolution absorption spectra of C₂ and CN. They derived $\dot{M} \approx 1.6 \times 10^{-6} M_{\odot} \text{yr}^{-1}$ from C₂ and $\dot{M} \approx 6.3 \times 10^{-6} M_{\odot} \text{yr}^{-1}$ from CN.³ Meixner et al. (1997) modeled the 9.7 and 11.8 μm images and the optical and IRAS photometry of this object, using a 2-dimensional axially symmetric dust code and amorphous carbon dust of a single size of $a = 0.01 \mu\text{m}$. They derived $\dot{M} \approx 1.3 \times 10^{-5} M_{\odot} \text{yr}^{-1}$ for $d = 4$ kpc and $M_{\text{gas}}/M_{\text{dust}} \approx 222$ (Jura 1986). This becomes $\dot{M} \approx 3.1 \times 10^{-5} M_{\odot} \text{yr}^{-1}$ for our adopted $d = 5.5$ kpc and $M_{\text{gas}}/M_{\text{dust}} = 280$. Sahai (1999) obtained the scattered light images of this source at 0.56 and 0.81 μm using the *Wide Field Planetary Camera 2* (WFPC2) on board the *Hubble Space Telescope* (HST). They derived a mass loss rate of $\dot{M} \approx 8 \times 10^{-6} M_{\odot} \text{yr}^{-1}$ for $d = 4.0$ kpc and $M_{\text{gas}}/M_{\text{dust}} \approx 200$, which corresponds to $\dot{M} \approx 1.75 \times 10^{-5} M_{\odot} \text{yr}^{-1}$ if our $d = 5.0$ kpc and $M_{\text{gas}}/M_{\text{dust}} = 280$ are adopted. Bujarrabal et al. (2001) derived $\dot{M} \approx 4.0 \times 10^{-5} M_{\odot} \text{yr}^{-1}$ based on the CO $J = 1 - 0$ and $J = 2 - 1$ emission lines. Hrivnak & Bieging (2005) estimated $\dot{M} \approx 3.6 \times 10^{-5} M_{\odot} \text{yr}^{-1}$ for $d = 5.4$ kpc from the CO $J = 2 - 1$ emission line observed with *HHT*, corresponding to $\dot{M} \approx 3.1 \times 10^{-5} M_{\odot} \text{yr}^{-1}$ for our adopted $d = 5.0$ kpc.

IRAS 05113+1347: This object is a carbon-rich G8Ia post-AGB star (Hrivnak 1995). We derive a mass loss rate of $\dot{M} \approx 2.59 \times 10^{-5} M_{\odot} \text{yr}^{-1}$ in the AGB phase. Bakker et al. (1997) derived $\dot{M} \approx 7.9 \times 10^{-7} M_{\odot} \text{yr}^{-1}$ from C₂ and $\dot{M} \approx 7.9 \times 10^{-6} M_{\odot} \text{yr}^{-1}$ from CN (see Footnote 3). Hrivnak et al. (2009) modeled the IR photometry up to $\lambda = 100 \mu\text{m}$ obtained by *MSX* and *IRAS* and the 10–36 μm *Spitzer*/IRS spectrum of this source using DUSTCD. Assuming $M_{\text{gas}}/M_{\text{dust}} = 330$ and adopting $d = 7.0$ kpc, they derived $\dot{M} \approx 3.2 \times 10^{-4} M_{\odot} \text{yr}^{-1}$, corresponding to a mass loss rate of $\dot{M} \approx 2.7 \times 10^{-4} M_{\odot} \text{yr}^{-1}$ for our adopted $d = 7.0$ kpc and $M_{\text{gas}}/M_{\text{dust}} = 280$. Reddy & Parthasarathy (1996) derived $\dot{M} \approx 4.6 \times 10^{-7} M_{\odot} \text{yr}^{-1}$ for $d = 5.0$ kpc from the *IRAS* 60 μm flux. This corresponds to $\dot{M} \approx 9.0 \times 10^{-7} M_{\odot} \text{yr}^{-1}$ for our $d = 7.0$ kpc.

²Hrivnak & Bieging (2005) derived the CO density distribution to be $\rho_{\text{CO}}(r) \propto r^{-3}$. They adopted a number-density ratio of CO to H₂ of $n(\text{CO})/n(\text{H}_2) = 7.4 \times 10^{-4}$ and assumed that all of the hydrogen is in the molecular form. In the following paragraphs, unless otherwise stated, all of the hydrogen in the 21 μm sources is assumed to be in H₂.

³ They took the ratio of the number density of C₂ and CN to that of H₂ to be $n(\text{C}_2)/n(\text{H}_2) = 4 \times 10^{-6}$, $n(\text{CN})/n(\text{H}_2) = 3 \times 10^{-6}$, respectively.

IRAS 05341+0852: This source has a very extended, optically thin circumstellar envelope. Its visible image shows an elongated elliptical nebula around the central star (Ueta et al. 2000). We derive a mass loss rate of $\dot{M} \approx 1.01 \times 10^{-5} M_{\odot} \text{yr}^{-1}$ in the AGB phase. Bakker et al. (1997) derived $\dot{M} \approx 1.0 \times 10^{-6} M_{\odot} \text{yr}^{-1}$ from C_2 and $\dot{M} \approx 1.0 \times 10^{-5} M_{\odot} \text{yr}^{-1}$ from CN. Hrivnak et al. (2009) modeled the optical and IR photometry and the 10–36 μm Spitzer/IRS spectrum of this source using DUSTCD. Assuming $M_{\text{gas}}/M_{\text{dust}} = 330$ and adopting $d = 8.2 \text{ kpc}$, they derived $\dot{M} \approx 1.0 \times 10^{-4} M_{\odot} \text{yr}^{-1}$, corresponding to a mass loss rate of $\dot{M} \approx 7.68 \times 10^{-5} M_{\odot} \text{yr}^{-1}$ for our adopted $d = 7.8 \text{ kpc}$ and $M_{\text{gas}}/M_{\text{dust}} = 280$. Reddy & Parthasarathy (1996) derived $\dot{M} \approx 2.7 \times 10^{-7} M_{\odot} \text{yr}^{-1}$ from the *IRAS* 60 μm flux for $d = 10.0 \text{ kpc}$. This becomes $\dot{M} \approx 1.6 \times 10^{-7} M_{\odot} \text{yr}^{-1}$ with our $d = 7.8 \text{ kpc}$.

IRAS 06530-0213: This object is a carbon rich F15Ib post-AGB star with a metal poor environment (Hrivnak & Reddy 2003). Its *HST* optical scattered-light image shows an elliptical reflection nebula (Ueta et al. 2000). We derive a mass loss rate of $\dot{M} \approx 1.86 \times 10^{-5} M_{\odot} \text{yr}^{-1}$ in the AGB phase. Reddy & Parthasarathy (1996) derived $\dot{M} \approx 1.8 \times 10^{-7} M_{\odot} \text{yr}^{-1}$ from the *IRAS* 60 μm flux for $d = 3.0 \text{ kpc}$. This corresponds to $\dot{M} \approx 4.42 \times 10^{-7} M_{\odot} \text{yr}^{-1}$ for our $d = 4.7 \text{ kpc}$. Hrivnak et al. (2009) modeled the *MSX* and *IRAS* photometry and the 10–36 μm Spitzer/IRS spectrum of this source using DUSTCD. Assuming $M_{\text{gas}}/M_{\text{dust}} = 330$ and adopting $d = 5.4 \text{ kpc}$, they derived $\dot{M} \approx 1.2 \times 10^{-4} M_{\odot} \text{yr}^{-1}$, corresponding to a mass loss rate of $\dot{M} \approx 7.71 \times 10^{-5} M_{\odot} \text{yr}^{-1}$ for our adopted $d = 4.7 \text{ kpc}$ and $M_{\text{gas}}/M_{\text{dust}} = 280$. Hrivnak & Bieging (2005) estimated $\dot{M} \approx 6.9 \times 10^{-5} M_{\odot} \text{yr}^{-1}$ from the CO $J = 2 - 1$ emission line observed with *HHT* for $d = 6.8 \text{ kpc}$. This corresponds to $\dot{M} \approx 3.3 \times 10^{-5} M_{\odot} \text{yr}^{-1}$ when our $d = 4.7 \text{ kpc}$ is adopted.

IRAS 07134+1005 (HD 56126): This source is one of the best studied post-AGB star. The circumstellar envelope around this star has an axial symmetric structure (Meixner et al. 1997; Ueta et al. 2000). It is one of the sources in which the 21 μm and 30 μm features were first discovered (Forrest et al. 1981, Kwok et al. 1989). Our model fits all the observed SED from the optical to the millimeter with 2-DUST. The 2-DUST model gives a mass loss rate of $\dot{M} \approx 1.99 \times 10^{-5} M_{\odot} \text{yr}^{-1}$ in the AGB phase. Assuming $n(\text{CO})/n(\text{H}_2) = 1 \times 10^{-3}$, Omont et al. (1993) estimated $\dot{M} \approx 9.7 \times 10^{-6} M_{\odot} \text{yr}^{-1}$ at $d = 2.4 \text{ kpc}$ from the CO $J = 2 - 1$ line. Hrivnak et al. (2000) modeled the 2–45 μm ISO spectrum of this source using DUSTCD. Assuming $M_{\text{gas}}/M_{\text{dust}} = 330$, they derived $\dot{M} / \{(v_{\text{exp}}/\text{km s}^{-1}) \times (d/\text{kpc})\} \approx 7.2 \times 10^{-7} M_{\odot} \text{yr}^{-1}$, corresponding to a mass loss rate of $\dot{M} \approx 1.47 \times 10^{-5} M_{\odot} \text{yr}^{-1}$ for our adopted $d = 2.4 \text{ kpc}$, $v_{\text{exp}} = 10.0 \text{ km s}^{-1}$, and $M_{\text{gas}}/M_{\text{dust}} = 280$. Hony et al. (2003) modeled the optical and *IRAS* photometry and the *ISO/SWS* and *ISO/LWS* spectra of this object using the MODUST radiative transfer code (Bouwman et al. 2000). They derived $\dot{M} \approx 1 \times 10^{-4} M_{\odot} \text{yr}^{-1}$ for $M_{\text{gas}}/M_{\text{dust}} = 220$ and $d = 2.4 \text{ kpc}$. This corresponds to $\dot{M} \approx 1.2 \times 10^{-4} M_{\odot} \text{yr}^{-1}$ for our $M_{\text{gas}}/M_{\text{dust}} = 280$ at $d = 2.4 \text{ kpc}$. Meixner et al. (2004) imaged the circumstellar envelope

of this object at the CO $J = 1 - 0$ line using the Berkeley-Illinois-Maryland Association (BIMA) millimeter array. They modeled the CO $J = 1 - 0$ BIMA images and the CO $J = 2 - 1$ (Knapp et al. 1998) and $J = 4 - 3$ (Knapp et al. 2000) line profiles, using the radiative transfer code of Justtanont et al. (1994). Assuming $n(\text{CO})/n(\text{H}_2) = 9.2 \times 10^{-4}$, they derived $\dot{M} \approx 5.1 \times 10^{-6} M_\odot \text{yr}^{-1}$ for the AGB wind. They also modeled the optical and IRAS photometry and the ISO spectrum of this source with 2-DUST. They derived a dust mass loss rate of $\dot{M}_{\text{dust}} \approx 9.6 \times 10^{-8} M_\odot \text{yr}^{-1}$ for the AGB wind. If we assume a gas-to-dust ratio of 280 (Justtanont et al. 1996), the AGB wind mass loss rate would be $\dot{M} \approx 2.7 \times 10^{-5} M_\odot \text{yr}^{-1}$, higher than that derived from CO by a factor of ~ 5.3 . Hrivnak & Bieging (2005) estimated $\dot{M} \approx 2.3 \times 10^{-5} M_\odot \text{yr}^{-1}$ from the CO $J = 4 - 3$ and $J = 2 - 1$ emission lines observed with *HHT*. Buemi et al. (2007) used DUSTY to model the SED from the optical to the millimeter and derived $\dot{M} \approx 3.48 \times 10^{-5} M_\odot \text{yr}^{-1}$ for $M_{\text{gas}}/M_{\text{dust}} = 220$ at $d = 2.4$ kpc. This becomes $\dot{M} \approx 4.43 \times 10^{-5} M_\odot \text{yr}^{-1}$ for our adopted $M_{\text{gas}}/M_{\text{dust}} = 280$ also at $d = 2.4$ kpc.

IRAS 07430+1115: This object shows an approximately centrosymmetric pattern as revealed by the near-IR J - and K -band polarimetric images obtained with the 3.8 m *United Kingdom Infrared Telescope* (UKIRT; Gledhill 2005). We derive a mass loss rate of $\dot{M} \approx 5.78 \times 10^{-5} M_\odot \text{yr}^{-1}$ in the AGB phase. Hrivnak et al. (2009) modeled the optical and IR photometry (of *MSX* and *IRAS*) and the 10–36 μm Spitzer/IRS spectrum of this source using DUSTCD. With $M_{\text{gas}}/M_{\text{dust}} = 330$ and $d = 6.7$ kpc, they derived $\dot{M} \approx 1.1 \times 10^{-3} M_\odot \text{yr}^{-1}$, corresponding to a mass loss rate of $\dot{M} \approx 7.48 \times 10^{-4} M_\odot \text{yr}^{-1}$ for our adopted $d = 6.0$ kpc and $M_{\text{gas}}/M_{\text{dust}} = 280$.

IRAS 14429-4539: We derive a mass loss rate of $\dot{M} \approx 3.22 \times 10^{-5} M_\odot \text{yr}^{-1}$ in the AGB phase. Reddy & Parthasarathi (1996) estimated the mass loss rate to be $\dot{M} \approx 3.8 \times 10^{-7} M_\odot \text{yr}^{-1}$ for $d = 6.0$ kpc based on the simple formula of Reimers (1975): $\dot{M} \propto L_\star^{1.5} T_\star^{-2} M_\star^{-1}$.

IRAS 16594-4656: This object is a bipolar post-AGB star as indicated by its SED (Meixner et al. 1999, Hrivnak et al. 2008). It has an optically thick circumstellar envelope. We derive a mass loss rate of $\dot{M} \approx 8.17 \times 10^{-5} M_\odot \text{yr}^{-1}$ in the AGB phase. Hrivnak et al. (2000) modeled the 2–45 μm ISO spectrum of this source using DUSTCD. Assuming $M_{\text{gas}}/M_{\text{dust}} = 330$ they derived $\dot{M} / \{(v_{\text{exp}}/\text{km s}^{-1}) \times (d/\text{kpc})\} \approx 3.9 \times 10^{-6} M_\odot \text{yr}^{-1}$, corresponding to a mass loss rate of $\dot{M} \approx 1.27 \times 10^{-4} M_\odot \text{yr}^{-1}$ for our adopted $d = 2.4$ kpc, $v_{\text{exp}} = 16.0 \text{ km s}^{-1}$, and $M_{\text{gas}}/M_{\text{dust}} = 280$.

IRAS 19477+2401: This source appears as a bipolar reflection nebula in the *UKIRT* J -band polarimetric image of scattered-light (Gledhill et al. 2001). We derive a mass loss rate of $\dot{M} \approx 2.37 \times 10^{-5} M_\odot \text{yr}^{-1}$ in the AGB phase. Hrivnak et al. (2000) modeled the 2–45 μm ISO spectrum of this source using DUSTCD. Assuming $M_{\text{gas}}/M_{\text{dust}} = 330$, they derived $\dot{M} / \{(v_{\text{exp}}/\text{km s}^{-1}) \times (d/\text{kpc})\} \approx 2.5 \times 10^{-6} M_\odot \text{yr}^{-1}$, corresponding to a mass loss

rate of $\dot{M} \approx 1.52 \times 10^{-4} M_{\odot} \text{yr}^{-1}$ for our adopted $d = 5.5 \text{ kpc}$, $v_{\text{exp}} = 13.0 \text{ km s}^{-1}$, and $M_{\text{gas}}/M_{\text{dust}} = 280$.

IRAS 19500-1709: This object shows a bipolar structure in the J - and K -band scattered-light polarimetric images of *UKIRT* (Gledhill et al. 2001). We derive a mass loss rate of $\dot{M} \approx 7.14 \times 10^{-5} M_{\odot} \text{yr}^{-1}$ in the AGB phase. Assuming $n(\text{CO})/n(\text{H}_2) = 1 \times 10^{-3}$, Likkell et al. (1991) derived $\dot{M}/(d/\text{kpc})^2 \approx 1.2 \times 10^{-6} M_{\odot} \text{yr}^{-1}$, corresponding to a mass loss rate of $\dot{M} \approx 2.02 \times 10^{-5} M_{\odot} \text{yr}^{-1}$ for our adopted $d = 4.1 \text{ kpc}$. Meixner et al. (1997) modeled the 9.7 and $11.8 \mu\text{m}$ images and the optical and IRAS photometry of this object, using a 2-dimensional axially symmetric dust code and amorphous carbon dust of a single size of $a = 0.01 \mu\text{m}$. They derived $\dot{M} \approx 1.3 \times 10^{-5} M_{\odot} \text{yr}^{-1}$ for $d = 2 \text{ kpc}$ and $M_{\text{gas}}/M_{\text{dust}} \approx 222$ (Jura 1986). This becomes $\dot{M} \approx 6.89 \times 10^{-5} M_{\odot} \text{yr}^{-1}$ for our adopted $d = 4.1 \text{ kpc}$ and $M_{\text{gas}}/M_{\text{dust}} = 280$. Assuming $n(\text{CO})/n(\text{H}_2) = 1 \times 10^{-3}$, Omont et al. (1993) estimated $\dot{M} \approx 8.0 \times 10^{-6} M_{\odot} \text{yr}^{-1}$ at $d = 2.1 \text{ kpc}$ from the CO $J = 2 - 1$ line. This becomes $\dot{M} \approx 3.05 \times 10^{-5} M_{\odot} \text{yr}^{-1}$ for our adopted $d = 4.1 \text{ kpc}$. Assuming $M_{\text{gas}}/M_{\text{dust}} = 223$, Clube & Gledhill (2004) derived $\dot{M} \approx 6.8 \times 10^{-5} M_{\odot} \text{yr}^{-1}$ for $d = 4.0 \text{ kpc}$ from fitting the near-, mid- and far-IR emission of this source. This becomes $\dot{M} \approx 8.97 \times 10^{-5} M_{\odot} \text{yr}^{-1}$ for our adopted $d = 4.1 \text{ kpc}$ and $M_{\text{gas}}/M_{\text{dust}} = 280$. Hrivnak & Bieging (2005) estimated $\dot{M} \approx 3.2 \times 10^{-5} M_{\odot} \text{yr}^{-1}$ for $d = 2.4 \text{ kpc}$ from the CO $J = 2 - 1$ emission line observed with *HHT*, corresponding to $\dot{M} \approx 9.33 \times 10^{-5} M_{\odot} \text{yr}^{-1}$ for our adopted $d = 4.1 \text{ kpc}$.

IRAS 20000+3239: The near-IR imaging polarimetry of this object clearly reveals an extended and axisymmetric bipolar structure (Gledhill et al. 2001). Our model estimates $\dot{M} \approx 2.32 \times 10^{-5} M_{\odot} \text{yr}^{-1}$ in the AGB phase. Assuming $n(\text{CO})/n(\text{H}_2) = 1 \times 10^{-3}$, Likkell et al. (1991) derived $\dot{M}/(d/\text{kpc})^2 \approx 1.1 \times 10^{-6} M_{\odot} \text{yr}^{-1}$, corresponding to a mass loss rate of $\dot{M} \approx 5.52 \times 10^{-6} M_{\odot} \text{yr}^{-1}$ for our adopted $d = 2.24 \text{ kpc}$. Hrivnak et al. (2000) modeled the $2\text{--}45 \mu\text{m}$ ISO spectrum of this source using DUSTCD. Assuming $M_{\text{gas}}/M_{\text{dust}} = 330$ they derived $\dot{M}/\{(v_{\text{exp}}/\text{km s}^{-1}) \times (d/\text{kpc})\} \approx 5.1 \times 10^{-7} M_{\odot} \text{yr}^{-1}$, corresponding to a mass loss rate of $\dot{M} \approx 1.16 \times 10^{-5} M_{\odot} \text{yr}^{-1}$ for our adopted $d = 2.24 \text{ kpc}$, $v_{\text{exp}} = 12.0 \text{ km s}^{-1}$, and $M_{\text{gas}}/M_{\text{dust}} = 280$. Buemi et al. (2007) used DUSTY to model the SED from the optical to the millimeter and derived $\dot{M} \approx 6.92 \times 10^{-6} M_{\odot} \text{yr}^{-1}$ for $M_{\text{gas}}/M_{\text{dust}} = 220$. This becomes $\dot{M} \approx 3.47 \times 10^{-5} M_{\odot} \text{yr}^{-1}$ for our adopted $M_{\text{gas}}/M_{\text{dust}} = 280$ and $d = 2.24 \text{ kpc}$. Assuming $n(\text{CO})/n(\text{H}_2) = 1 \times 10^{-3}$, Omont et al. (1993) estimated $\dot{M} \approx 1.2 \times 10^{-5} M_{\odot} \text{yr}^{-1}$ at $d = 5.5 \text{ kpc}$ from the CO $J = 2 - 1$ line. This becomes $\dot{M} \approx 1.99 \times 10^{-6} M_{\odot} \text{yr}^{-1}$ for our adopted $d = 2.24 \text{ kpc}$.

IRAS 22223+4327: The near-IR imaging polarimetry of this object reveals an extended scattering envelope that is optically thick and illuminated by the central star (Gledhill et al. 2001). We derive a mass loss rate of $\dot{M} \approx 2.18 \times 10^{-5} M_{\odot} \text{yr}^{-1}$ in the AGB phase. Assuming

$n(\text{CO})/n(\text{H}_2) = 1 \times 10^{-3}$, Likkell et al. (1991) derived $\dot{M}/(d/\text{kpc})^2 \approx 6.0 \times 10^{-7} M_\odot \text{yr}^{-1}$, corresponding to a mass loss rate of $\dot{M} \approx 6.14 \times 10^{-6} M_\odot \text{yr}^{-1}$ for our adopted $d = 3.2 \text{ kpc}$. Bakker et al. (1997) derived $\dot{M} \approx 2.5 \times 10^{-5} M_\odot \text{yr}^{-1}$ from C_2 and $\dot{M} \approx 1.6 \times 10^{-4} M_\odot \text{yr}^{-1}$ from CN (see Footnote 3).

IRAS 22272+5435: This source is extremely carbon-rich and fairly bright both in the IR and optical (Ueta et al. 2001). We derive $\dot{M} \approx 2.59 \times 10^{-6} M_\odot \text{yr}^{-1}$ for the AGB wind. Bujarrabal et al. (2001) derived $\dot{M} \approx 2.0 \times 10^{-5} M_\odot \text{yr}^{-1}$ based on the $\text{CO } J = 1 - 0$ and $J = 2 - 1$ emission lines. for $d = 1.7 \text{ kpc}$. This becomes $\dot{M} \approx 1.88 \times 10^{-5} M_\odot \text{yr}^{-1}$ for our adopted $d = 1.65 \text{ kpc}$. Hrivnak & Bieging (2005) estimated $\dot{M} \approx 7.7 \times 10^{-5} M_\odot \text{yr}^{-1}$ for $d = 1.9 \text{ kpc}$ from the $\text{CO } J = 2 - 1$ emission line observed with *HHT*, corresponding to $\dot{M} \approx 5.8 \times 10^{-5} M_\odot \text{yr}^{-1}$ for our adopted $d = 1.65 \text{ kpc}$. Buemi et al. (2007) used DUSTY to model the SED from the optical to the millimeter and derived $\dot{M} \approx 3.12 \times 10^{-5} M_\odot \text{yr}^{-1}$ for $M_{\text{gas}}/M_{\text{dust}} = 220$. This becomes $\dot{M} \approx 4.2 \times 10^{-5} M_\odot \text{yr}^{-1}$ for our adopted $M_{\text{gas}}/M_{\text{dust}} = 280$ and $d = 1.65 \text{ kpc}$.

IRAS 22574+6609: This object is very faint in the visible. It shows a bipolar morphology with a dark lane dividing the nebula into two lobes (Ueta et al. 2000; Su et al. 2001). We derive a mass loss rate of $\dot{M} \approx 3.39 \times 10^{-4} M_\odot \text{yr}^{-1}$ in the AGB phase. Assuming $n(\text{CO})/n(\text{H}_2) = 1 \times 10^{-3}$, Likkell et al. (1991) derived $\dot{M}/(d/\text{kpc})^2 \approx 2.0 \times 10^{-6} M_\odot \text{yr}^{-1}$, corresponding to a mass loss rate of $\dot{M} \approx 1.15 \times 10^{-4} M_\odot \text{yr}^{-1}$ for our adopted $d = 7.6 \text{ kpc}$. Hrivnak et al. (2000) modeled the $2\text{--}45 \mu\text{m}$ ISO spectrum of this source using DUSTCD. Assuming $M_{\text{gas}}/M_{\text{dust}} = 330$ they derived $\dot{M}/\{(v_{\text{exp}}/\text{km s}^{-1}) \times (d/\text{kpc})\} \approx 3.2 \times 10^{-7} M_\odot \text{yr}^{-1}$, corresponding to a mass loss rate of $\dot{M} \approx 3.3 \times 10^{-5} M_\odot \text{yr}^{-1}$ for our adopted $d = 7.6 \text{ kpc}$, $v_{\text{exp}} = 16.0 \text{ km s}^{-1}$, and $M_{\text{gas}}/M_{\text{dust}} = 280$. Hrivnak & Bieging (2005) estimated $\dot{M} \approx 1.4 \times 10^{-4} M_\odot \text{yr}^{-1}$ for $d = 7.7 \text{ kpc}$ from the $\text{CO } J = 2 - 1$ emission line observed with *HHT*, corresponding to $\dot{M} \approx 1.36 \times 10^{-4} M_\odot \text{yr}^{-1}$ for our adopted $d = 7.6 \text{ kpc}$.

IRAS 23304+6147: We derive a mass loss rate of $\dot{M} \approx 2.39 \times 10^{-5} M_\odot \text{yr}^{-1}$ in the AGB phase. Assuming $n(\text{CO})/n(\text{H}_2) = 1 \times 10^{-3}$, Likkell et al. (1991) derived $\dot{M}/(d/\text{kpc})^2 \approx 1.2 \times 10^{-6} M_\odot \text{yr}^{-1}$, corresponding to a mass loss rate of $\dot{M} \approx 1.33 \times 10^{-5} M_\odot \text{yr}^{-1}$ for our adopted $d = 3.25 \text{ kpc}$. Assuming $n(\text{CO})/n(\text{H}_2) = 1 \times 10^{-3}$, Omont et al. (1993) estimated $\dot{M} \approx 1.8 \times 10^{-5} M_\odot \text{yr}^{-1}$ at $d = 2.4 \text{ kpc}$ from the $\text{CO } J = 2 - 1$ line. This becomes $\dot{M} \approx 3.3 \times 10^{-5} M_\odot \text{yr}^{-1}$ for our adopted $d = 3.25 \text{ kpc}$. Bakker et al. (1997) derived $\dot{M} \approx 1.0 \times 10^{-5} M_\odot \text{yr}^{-1}$ from C_2 and $\dot{M} \approx 5.0 \times 10^{-5} M_\odot \text{yr}^{-1}$ from CN (see Footnote 3). Hrivnak & Bieging (2005) estimated $\dot{M} \approx 2.9 \times 10^{-4} M_\odot \text{yr}^{-1}$ for $d = 4.7 \text{ kpc}$ from the $\text{CO } J = 2 - 1$ emission line observed with *HHT*, corresponding to $\dot{M} \approx 1.4 \times 10^{-5} M_\odot \text{yr}^{-1}$ for our adopted $d = 3.25 \text{ kpc}$.

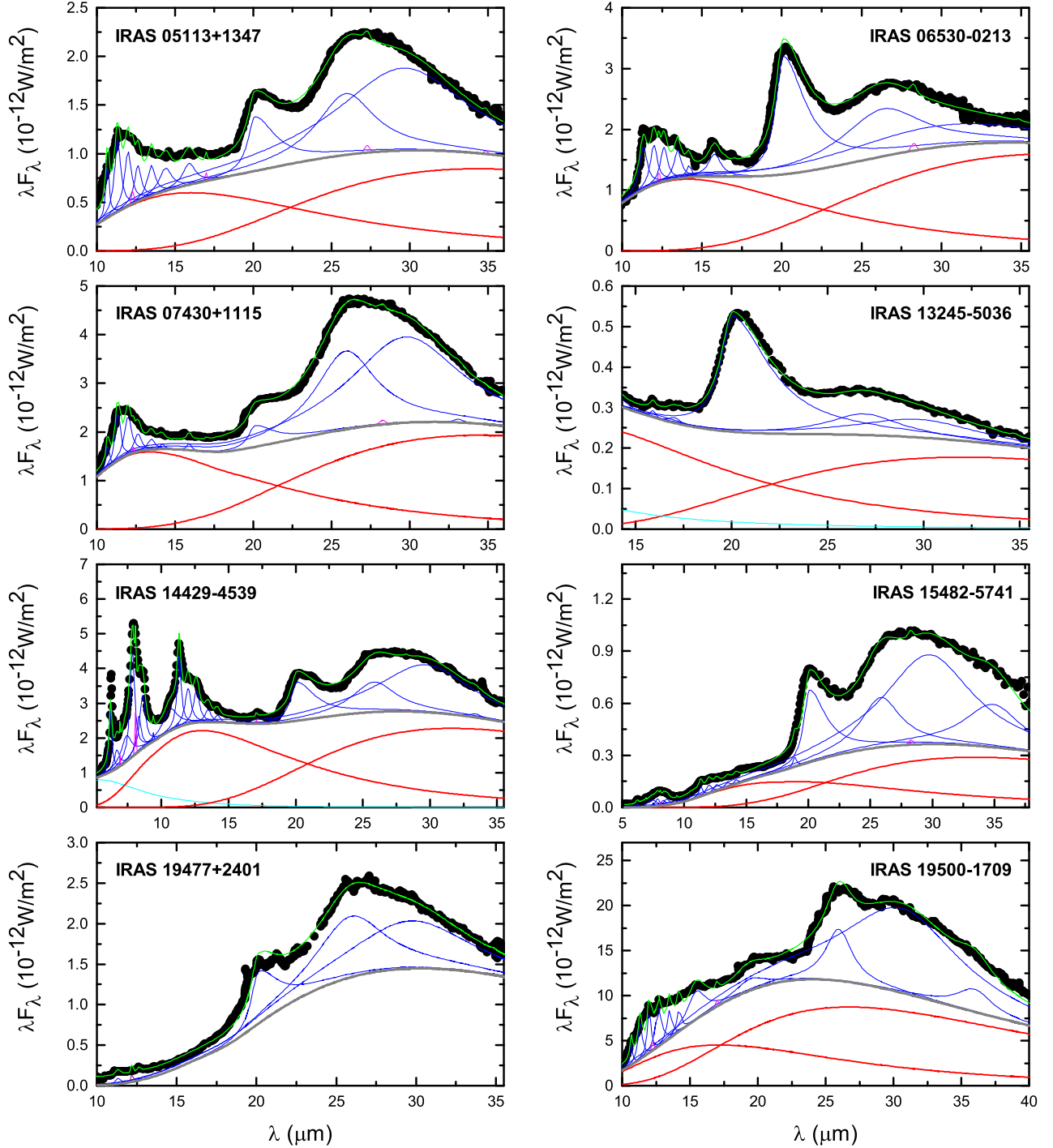


Fig. 1.— Decomposition of the observed IR spectra (black points) of eight $21\ \mu\text{m}$ sources (IRAS 05113+1347, IRAS 06530-0213, IRAS 07430+1115, IRAS 13245-5036, IRAS 14429-4539, IRAS 15482-5741, IRAS 19477+2401, and IRAS 19500-1709) into a stellar continuum (cyan line), two dust thermal continuum emission components (red lines), the 21 , $30\ \mu\text{m}$ and UIR features (blue lines), and the H_2 bands (magenta lines). The decomposition is done with the PAHFIT technique. Gray lines are the sum of the stellar and dust thermal continuum. Green lines show the resulting model spectra. For most sources (except IRAS 13245-5036 and IRAS 14429-4539), the stellar contribution is too weak to show up. For IRAS 19477+2401, there is only one dust continuum component and the stellar continuum is so small that the gray line (which plots the sum of the stellar and dust continuum) overlaps the red line (which plots the dust continuum).

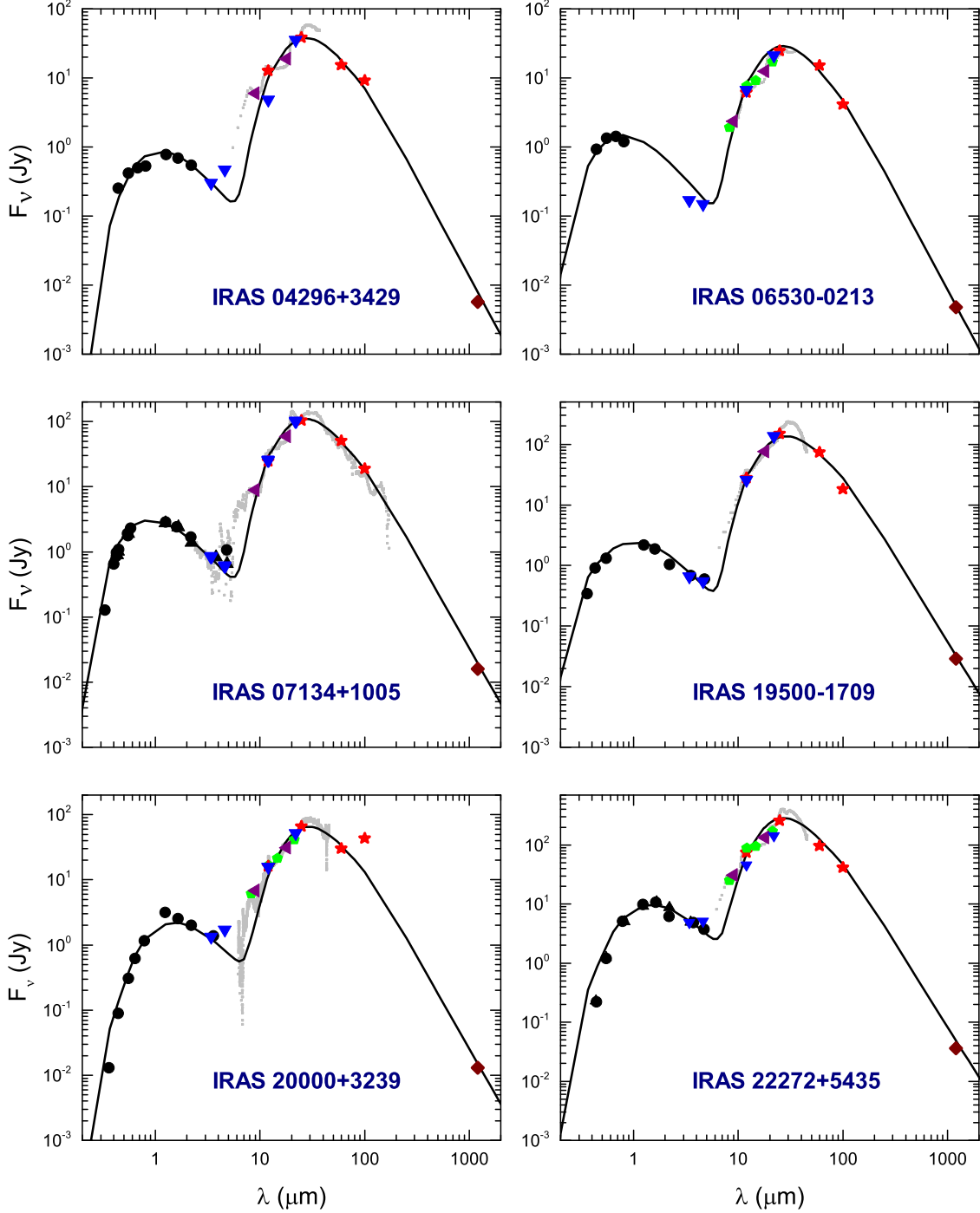


Fig. 2.— Comparison of the model SEDs with the broadband photometry of *IRAS* (red stars), *AKARI* (purple triangles), *WISE* (blue triangles), *MSX* (green pentagons), and the 1.2 mm *IRAM/MAMBO* data (wine diamonds), as well as the optical/near-IR stellar photospheric emission (filled circles) and the *ISO/SWS* or *Spitzer/IRS* mid-IR spectra (gray lines) for IRAS 04296+3426, IRAS 06530-0213, IRAS 07134+1005, IRAS 19500-1709, IRAS 20000+3239, and IRAS 22272+5435. The model SEDs were computed using the 2-DUST code of Ueta & Meixner (2003). We note that the contributions of the 21 and 30 μm features to the photometric fluxes of the *AKARI* 18 μm band, the *MSX* *E* band at 21.34 μm , the *WISE* 22 μm band, and the *IRAS* 25 μm band have been subtracted (see §3).

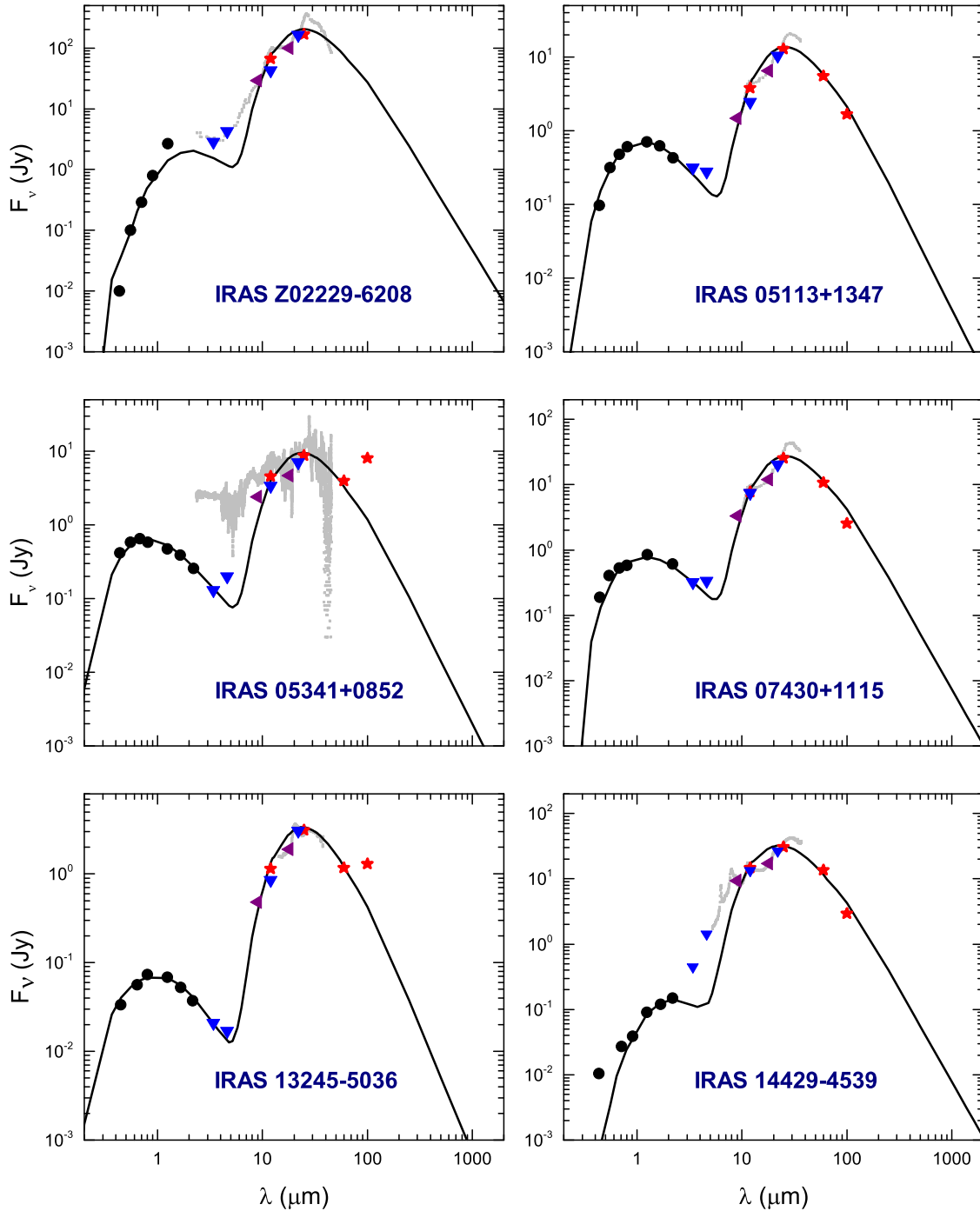


Fig. 3.— Comparison of the model SEDs with the broadband photometry of *IRAS* (red stars), *AKARI* (purple triangles), *WISE* (blue triangles), *MSX* (green pentagons), as well as the optical/near-IR stellar photospheric emission (filled circles) and the *ISO/SWS* or *Spitzer/IRS* mid-IR spectra (gray lines) for IRAS Z02229-6208, IRAS 05113+1347, IRAS 05341+0852, IRAS 07430+1115, IRAS 13245-5036, and IRAS 14429-4539. The contributions of the 21 and 30 μm features to the photometric fluxes of the *AKARI* 18 μm band, the *MSX* *E* band at 21.34 μm , the *WISE* 22 μm band, and the *IRAS* 25 μm band have been subtracted.

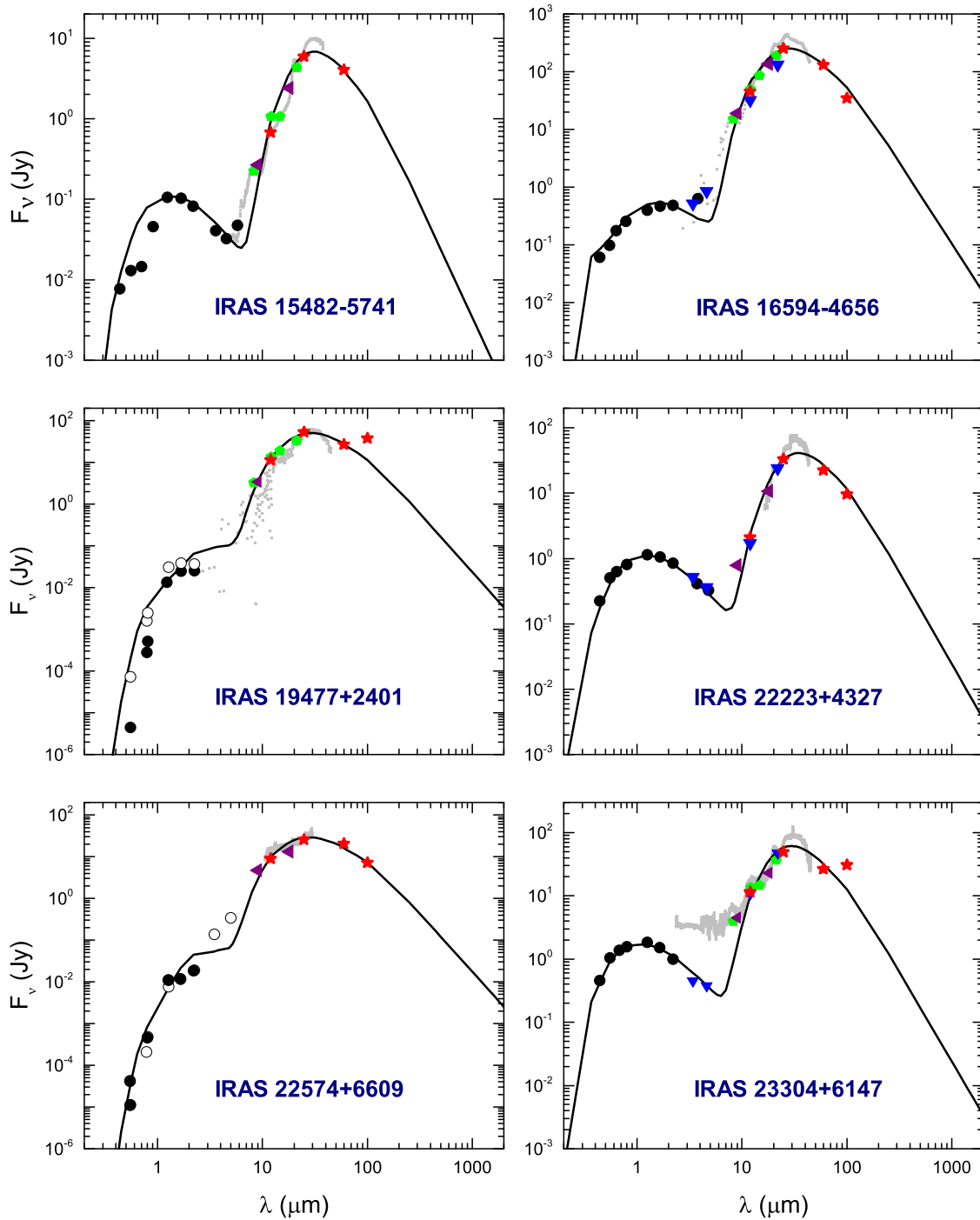


Fig. 4.— Same as Figure 3 but for IRAS 15482-5741, IRAS 16594-4656, IRAS 19477+2401, IRAS 22223+4327, IRAS 22574+6609, IRAS and IRAS 23304+6147.

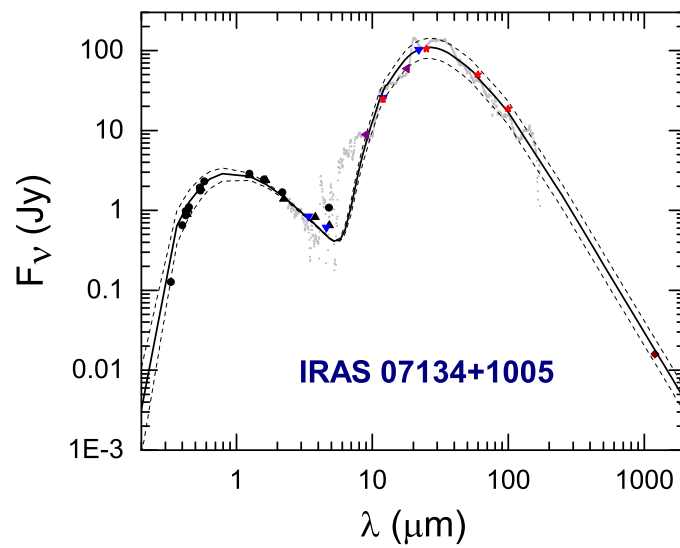


Fig. 5.— Determination of the uncertainty for $\tau_{9.8}$ for IRAS07134+1005. The data points plot the broadband photometry of *IRAS* (red stars), *AKARI* (purple triangles), *WISE* (blue triangles), *MSX* (green pentagons), as well as the optical/near-IR stellar photospheric emission (filled circles). The solid line plots the the best-fit model with $\tau_{9.8} \approx 0.022$, while the dashed lines correspond to the model SEDs obtained with $\tau_{9.8}$ set to the extremes of its allowable range: $\tau_{9.8} \approx 0.0146$ for the lower curve and $\tau_{9.8} \approx 0.0294$ for upper curve.

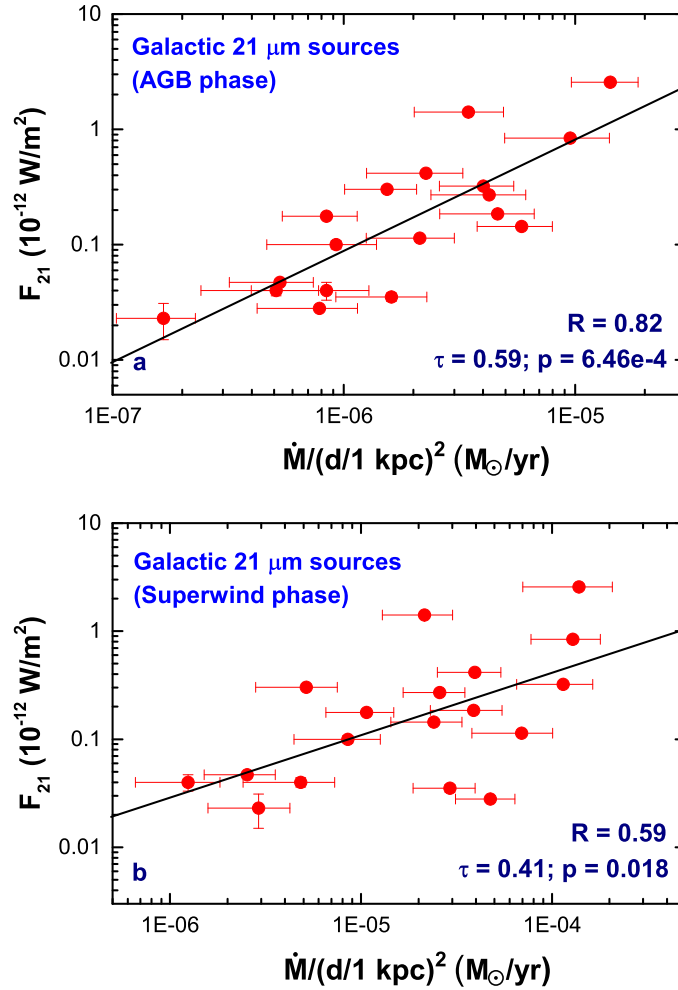


Fig. 6.— Correlation of the 21 μm feature with the stellar mass loss rates in the AGB phase (a) and in the superwind phase (b). Note that the error-bar sizes of F_{21} and F_{30} are smaller than that of the red circles.

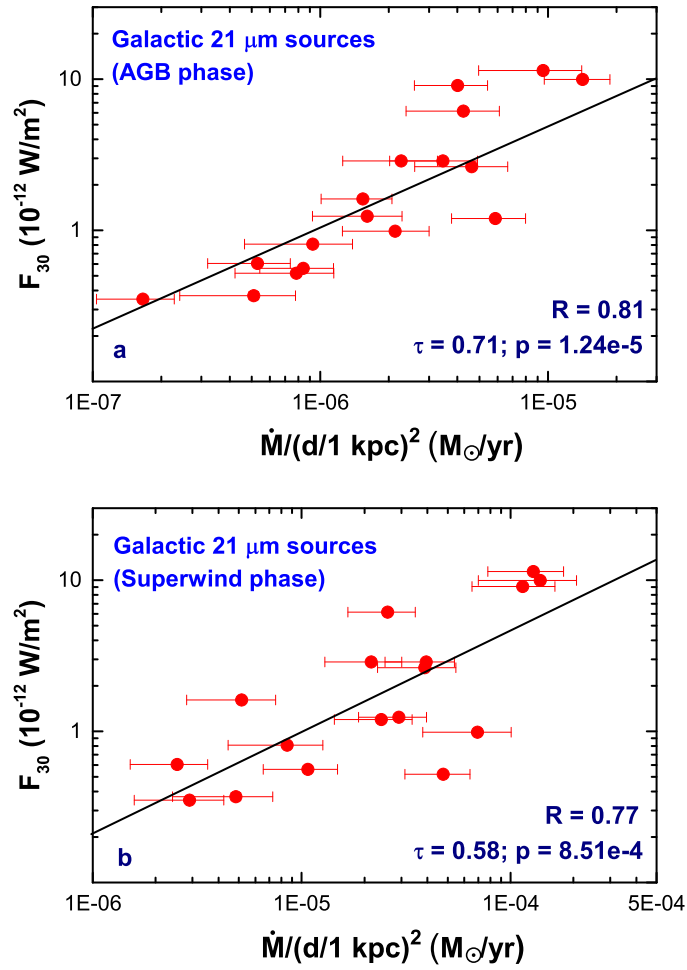


Fig. 7.— Correlation of the 30 μm feature with the stellar mass loss rates in the AGB (a) and superwind (b) phases.

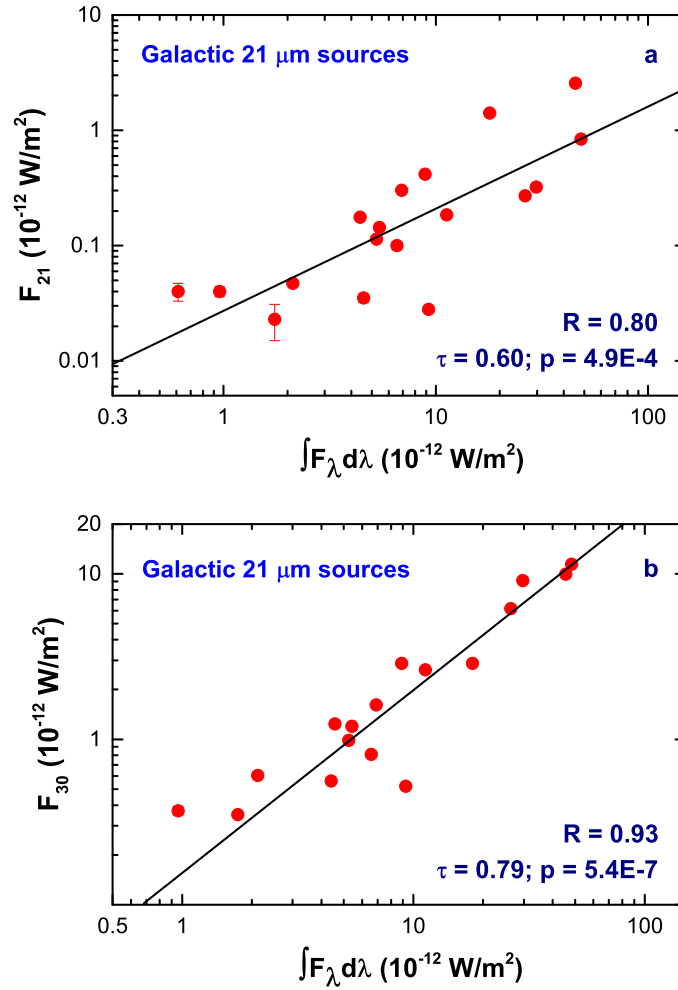


Fig. 8.— Correlation of the 21 μm feature (a) and the 30 μm feature (b) with the total IR emission obtained by integrating the observed dust IR SED over the entire wavelength range.

Table 1: Stellar Parameters and *IRAS*, *WISE*, *AKARI*, *MSX*, and *IRAM*/MAMBO 1.2 mm Photometry for 18 Galactic 21 μm Sources.

IRAS	T_{eff}	L_{\star}	M_{\star}	r_{\star}	d	<i>IRAS</i> (Jy)				<i>WISE</i> (Jy)				<i>AKARI</i> (Jy)		<i>MSX</i> (Jy)				<i>IRAM</i> (mJy)	
						12	25	60	100	3.4	4.6	12	22	9	18	8.28	12.13	14.65	21.34		1.2
Sources	(K)	(L_{\odot})	(M_{\odot})	(R_{\odot})	(kpc)	(μm)	(μm)	(μm)	(μm)	(μm)	(μm)	(μm)	(μm)	(μm)	(μm)	(μm)	(μm)	(μm)	(μm)	(mm)	
Z02229+6208	5500	8470	0.558	98.4	2.20	66.7	203.6	3.6	...	2.88	4.27	42.54	168.48	29.05	110.80	
04296+3429	6500	8334	0.554	69.1	5.00	12.7	45.9	15.5	9.22	0.30	0.47	4.85	36.25	5.99	22.33	4.4 \pm 1.3
05113+1347	5500	8315	0.604	97.5	7.00	3.78	15.3	5.5	1.67	0.32	0.28	2.45	10.68	1.48	7.60
05341+0852	6500	8430	0.551	69.5	7.80	4.51	9.8	3.9	8.01	0.13	0.20	3.39	7.21	2.41	5.11
06530-0213	7000	8317	0.560	59.3	4.70	6.11	27.4	15.1	4.10	0.17	0.15	6.73	21.70	2.37	13.84	1.91	7.66	9.13	18.49	4.8 \pm 1.5	
07134+1005	7250	6555	0.841	49.0	2.40	24.5	116.7	50.1	18.7	0.84	0.61	25.74	104.46	8.91	66.25	14.0 \pm 1.5
07430+1115	5500	8318	<0.550	97.5	6.00	7.68	29.9	10.7	2.53	0.32	0.34	7.43	20.71	3.30	13.50
13245-5036	8500	2757	...	23.0	7.70	1.14	3.5	1.2	1.30	0.02	0.02	0.85	3.11	0.48	2.15
14429-4539	6500	8552	...	70.0	5.90	14.6	33.3	13.6	2.91	0.45	1.43	13.37	26.65	9.36	18.43
15482-5741	6500	3534	...	45.0	7.00	0.67	7.1	4.0	53.80	0.27	2.86	0.22	1.06	1.07	4.83
16594-4656	10000	10279	0.600	32.0	2.40	44.9	298.0	131.4	34.40	0.52	0.86	32.43	137.58	19.00	158	15.08	49.03	84.83	214.07
19477+2401	5500	8061	0.600	96.0	5.50	11.2	54.9	27.1	38.00	3.46	...	3.23	13.34	19.09	34.3
19500-1709	8000	25435	0.599	79.0	4.10	27.8	165.0	73.4	18.20	0.66	0.55	25.71	138.98	...	81.07	29.5
20000+3239	5500	5186	...	77.0	2.24	16.0	73.6	30.0	43.10	1.34	1.73	15.78	52.64	6.78	34.03	6.15	16.53	21.37	44.24	11.4 \pm 1.7	...
22223+4327	6500	6075	0.551	59.0	3.20	2.12	37.1	22.4	9.54	0.52	0.36	1.72	24.69	0.79	12.23
22272+5435	5650	10990	0.574	106.0	1.65	73.9	302.4	96.6	41.00	4.83	5.10	45.93	145.66	31.00	148.80	25.07	87.85	95.38	186.64	35.3 \pm 1.7	...
22574+6609	5500	8062	0.600	96.0	7.60	9.00	29.5	20.6	7.19	4.73	14.80
23304+6147	6750	8348	0.660	64.0	3.25	11.4	59.1	26.6	30.9	0.45	0.38	10.79	48.10	4.47	27.10	3.93	13.42	14.67	40.96

Table 2: Integrated Fluxes Emitted in the UIR (F_{UIR}), 21 μm (F_{21}), and 30 μm (F_{30}) Features as Derived from the PAHFIT Decomposition Method.

IRAS Sources	Warm Dust T_W (K)	Cold Dust T_C (K)	UIR ($10^{-12} \text{ W m}^{-2}$)	F_{21} ($10^{-12} \text{ W m}^{-2}$)	F_{30} ($10^{-12} \text{ W m}^{-2}$)
05113+1347	150	70	0.180±0.002	0.047±0.002	0.604±0.006
06530-0213	170	75	0.027±0.0006	0.177±0.005	0.558±0.004
07430+1115	180	70	0.218±0.003	0.035±0.003	1.236±0.007
13245-5036	196	75	...	0.040±0.007	0.031±0.006
14429-4539 ¹	185	76	1.194±0.01	0.099±0.008	0.810±0.021
15482-5741	130	72	0.046±0.005	0.040±0.004	0.370±0.023
19477+2401	...	80	0.007±0.0001	0.028±0.001	0.521±0.005
19500-1709	140	90	1.034±0.101	0.266±0.002	6.160±0.129

¹ A hot component of $T = 445 \text{ K}$ is added to fit the continuum at $\lambda < 10 \mu\text{m}$.

Table 3: Model Parameters for Fitting the Observed SEDs Using the 2-DUST Code.

IRAS Sources	r_{min} (10^{16} cm)	r_{sw} (10^{16} cm)	r_{max} (10^{17} cm)	$\tau_{9.8}^\dagger$	θ^\ddagger	v_{exp} (km s^{-1})	A	B	C	D	E	F	β
Z02229+6208	2.62±0.93 ¹	3.44±1.28 ²	1.71±0.41	0.156±0.0490	90 ^{o a}	14.8 ⁵	8.0	6.0	1.0	5.0	9.0	10.0	5.8
04296+3429	4.47±1.42 ²	13.0±4.18 ²	1.43±0.56	0.021±0.0064	45 ^{o b}	12.0 ⁶	2.0	4.0	3.0	6.0	7.0	15.0	4.1
05113+1347	4.28±1.21	6.10±2.14	1.71±0.44	0.010±0.0031	0 ^{o c}	13.1 ⁹	0.1	4.5	1.0	9.0	9.0	9.0	3.5
05341+0852	4.10±1.36	4.88±1.46	2.48±0.68	0.002±0.0005	80 ^{o c}	13.0 ⁵	0.01	6.0	9.0	3.0	9.0	9.0	3.9
06530-0213	4.62±1.59	6.01±1.99	2.77±0.99	0.004±0.0012	90 ^{o a}	14.0 ¹⁰	0.01	6.0	9.0	9.0	7.0	12.0	4.0
07134+1005	4.29±1.39 ³	6.44±2.20 ²	1.07±0.41 ³	0.027±0.0091	80 ^{o e}	10.0 ⁶	3.5	3.5	1.0	7.0	9.0	3.0	4.3
07430+1115	2.95±1.03	3.24±1.00	1.50±0.51	0.035±0.0089	90 ^{o c}	15.2 ⁹	0.05	7.0	2.0	7.0	9.0	20.0	5.4
13245-5036	2.52±1.01	3.27±1.46	0.51±0.24	0.016±0.0042	90 ^o	15.0	5.0	3.0	3.0	6.0	4.0	8.0	3.2
14429-4539	1.76±0.62	4.22±1.77	1.77±0.78	0.200±0.0551	90 ^o	18.2 ¹²	4.0	4.0	1.0	6.0	6.0	6.0	6.8
15482-5741	3.23±1.21	4.52±1.83	2.42±1.01	0.076±0.0258	90 ^o	15.0	9.0	4.0	1.0	1.0	4.0	26.0	6.2
16594-4656	5.01±1.38 ²	6.01±1.76 ²	2.80±0.92	0.134±0.0406	75 ^{o a}	16.0 ⁷	9.0	4.5	1.0	9.0	3.0	12.0	5.3
19477+2401	2.62±0.69	4.20±1.41	2.62±0.81	0.385±0.1033	60 ^{o d}	13.0 ⁵	5.0	6.5	3.0	6.0	9.0	3.0	4.5
19500-1709	10.5±3.64	11.5±3.87	4.72±1.63	0.030±0.0103	45 ^{o b}	11.0 ¹¹	8.0	3.5	1.0	1.0	4.0	9.0	4.0
20000+3239	3.34±0.87 ⁴	4.01±1.36	1.67±0.56 ⁴	0.076±0.0216	90 ^o	12.0 ⁶	12.0	4.5	1.0	3.0	1.0	12.0	5.3
22223+4327	7.15±2.21 ⁴	7.87±2.61	3.58±1.33 ⁴	0.055±0.0144	90 ^{o f}	14.0 ⁶	12.0	8.0	1.0	4.0	3.0	15.0	5.4
22272+5435	4.62±0.88	5.10±1.53	1.88±0.46	0.067±0.0221	45 ^{o b}	9.80 ⁵	12.0	5.5	1.0	1.0	1.0	15.0	4.9
22574+6609	2.04±0.58 ⁵	4.89±1.48	1.20±0.41	0.361±0.1176	90 ^{o d}	16.0 ⁸	2.0	4.0	3.0	4.0	5.0	9.0	4.8
23304+6147	5.33±1.44 ⁴	6.92±2.03	2.66±0.87 ⁴	0.039±0.0128	90 ^{o g}	15.5 ⁶	12.0	6.0	5.0	3.5	7.0	12.0	5.5

[†] Optical depth at 9.8 μm .

[‡] Inclination angle: ^a Ueta et al. (2005); ^b Meixner et al. (1997); ^c Ueta et al. (2000); ^d Su et al. (2001); ^e Meixner et al. (2004); ^f Hrivnak et al. (2011); ^g Bujarrabal et al. (2001).

¹ Kwok et al. (2002); ² Ueta et al. (2005); ³ Nakashima et al. (2009); ⁴ Sahai et al. (2007); ⁵ Hrivnak et al. (2000); ⁶ Bakker et al. (1997); ⁷ Loup et al. (1990); ⁸ Hrivnak & Kwok (1991); ⁹ Hrivnak & Kwok (1999); ¹⁰ Hrivnak & Reddy (2003); ¹¹ Likkell et al. (1987); ¹² Reddy & Parthasarathy (1996).

Table 4: Contributions of the 21 and 30 μm Features to the Photometric Fluxes of the *AKARI* 18 μm Band, the *MSX E* Band at 21.34 μm , the *WISE* 22 μm Band, and the *IRAS* 25 μm Band.

IRAS Sources	<i>IRAS</i> (25 μm) (Jy)	<i>WISE</i> (22 μm) (Jy)	<i>AKARI</i> (18 μm) (Jy)	<i>MSX</i> (21.34 μm) (Jy)
Z02229+6208	37.89	2.82	13.04	13.67
04296+3429	9.21	1.12	4.75	5.34
05113+1347	2.41	0.24	1.05	1.14
05341+0852	1.33	0.12	0.54	0.58
06530-0213	3.68	0.55	2.27	2.59
07134+1005	18.97	3.00	12.44	14.33
07430+1115	4.64	0.37	1.66	1.75
13245-5036	0.63	0.10	0.42	0.46
14429-4539	3.65	0.40	1.69	1.88
15482-5741	1.39	0.15	0.65	0.72
16594-4656	60.75	7.56	33.79	37.00
19477+2401	2.42	9.26	1.21	1.35
19500-1709	16.81	1.21	6.63	5.27
20000+3239	9.03	0.90	4.04	4.30
22223+4327	4.72	0.49	2.11	2.33
22272+5435	48.28	4.39	19.40	21.01
22574+6609	4.08	0.42	2.28	2.33
23304+6147	11.95	1.32	5.97	6.62

Table 5: Dust Mass (M_{dust}) and Stellar Mass Loss Rates (\dot{M}) in the AGB and SW Phases (Assuming a Gas-to-Dust Ratio of ~ 280 Appropriate for Carbon-Rich AGB Stars; Justtanont et al. 1996) as Derived from the 2-DUST Model of Ueta & Meixner (2003).

IRAS Sources	AGB			SW		
	\dot{M} ($M_{\odot} \text{ yr}^{-1}$)	M_{dust} (M_{\odot})	Duration (yr)	\dot{M} ($M_{\odot} \text{ yr}^{-1}$)	M_{dust} (M_{\odot})	Duration (yr)
Z02229+6208	$(1.94 \pm 0.68) \times 10^{-5}$	$(1.96 \pm 0.54) \times 10^{-4}$	$(2.83 \pm 0.89) \times 10^3$	$(5.53 \pm 2.36) \times 10^{-4}$	$(3.79 \pm 1.13) \times 10^{-4}$	$(1.92 \pm 0.50) \times 10^2$
04296+3429	$(3.84 \pm 1.32) \times 10^{-5}$	$(4.88 \pm 1.55) \times 10^{-5}$	$(3.55 \pm 0.92) \times 10^2$	$(1.29 \pm 0.58) \times 10^{-4}$	$(1.04 \pm 0.35) \times 10^{-3}$	$(2.25 \pm 0.67) \times 10^3$
05113+1347	$(2.59 \pm 1.02) \times 10^{-5}$	$(3.40 \pm 1.01) \times 10^{-4}$	$(3.67 \pm 0.86) \times 10^3$	$(1.24 \pm 0.49) \times 10^{-4}$	$(1.81 \pm 0.55) \times 10^{-4}$	$(4.08 \pm 1.25) \times 10^2$
05341+0852	$(1.01 \pm 0.37) \times 10^{-5}$	$(1.63 \pm 0.42) \times 10^{-4}$	$(4.53 \pm 1.09) \times 10^3$	$(1.77 \pm 0.81) \times 10^{-4}$	$(1.17 \pm 0.38) \times 10^{-4}$	$(1.85 \pm 0.59) \times 10^1$
06530-0213	$(1.86 \pm 0.66) \times 10^{-5}$	$(3.06 \pm 0.86) \times 10^{-4}$	$(4.61 \pm 1.01) \times 10^3$	$(2.36 \pm 0.92) \times 10^{-4}$	$(2.48 \pm 0.76) \times 10^{-4}$	$(2.94 \pm 0.62) \times 10^2$
07134+1005	$(1.99 \pm 0.83) \times 10^{-5}$	$(2.33 \pm 0.62) \times 10^{-4}$	$(1.36 \pm 0.31) \times 10^3$	$(1.24 \pm 0.50) \times 10^{-4}$	$(3.02 \pm 0.95) \times 10^{-4}$	$(6.82 \pm 1.75) \times 10^2$
07430+1115	$(5.78 \pm 2.45) \times 10^{-5}$	$(5.17 \pm 1.53) \times 10^{-4}$	$(2.50 \pm 0.62) \times 10^3$	$(1.05 \pm 0.38) \times 10^{-3}$	$(2.35 \pm 0.81) \times 10^{-4}$	$(6.26 \pm 1.50) \times 10^1$
13245-5036	$(4.98 \pm 2.39) \times 10^{-5}$	$(6.66 \pm 2.36) \times 10^{-5}$	$(3.75 \pm 1.21) \times 10^2$	$(7.36 \pm 3.45) \times 10^{-5}$	$(4.22 \pm 1.46) \times 10^{-5}$	$(1.61 \pm 0.51) \times 10^2$
14429-4539	$(3.22 \pm 1.63) \times 10^{-5}$	$(3.06 \pm 1.22) \times 10^{-4}$	$(2.65 \pm 0.83) \times 10^3$	$(2.97 \pm 1.42) \times 10^{-4}$	$(5.18 \pm 1.91) \times 10^{-4}$	$(4.89 \pm 1.49) \times 10^2$
15482-5741	$(2.50 \pm 1.31) \times 10^{-5}$	$(3.73 \pm 1.51) \times 10^{-4}$	$(4.18 \pm 1.41) \times 10^3$	$(2.37 \pm 1.19) \times 10^{-4}$	$(2.32 \pm 0.91) \times 10^{-4}$	$(2.74 \pm 0.86) \times 10^2$
16594-4656	$(8.17 \pm 2.62) \times 10^{-5}$	$(1.46 \pm 0.51) \times 10^{-3}$	$(5.01 \pm 1.23) \times 10^3$	$(7.98 \pm 3.93) \times 10^{-4}$	$(6.48 \pm 1.78) \times 10^{-4}$	$(2.27 \pm 0.62) \times 10^2$
19477+2401	$(2.37 \pm 1.09) \times 10^{-5}$	$(4.57 \pm 1.21) \times 10^{-4}$	$(5.39 \pm 1.33) \times 10^3$	$(1.44 \pm 0.49) \times 10^{-3}$	$(1.99 \pm 0.66) \times 10^{-3}$	$(3.85 \pm 0.96) \times 10^2$
19500-1709	$(7.14 \pm 3.14) \times 10^{-5}$	$(2.64 \pm 0.76) \times 10^{-3}$	$(1.03 \pm 0.26) \times 10^4$	$(4.34 \pm 1.54) \times 10^{-4}$	$(4.72 \pm 1.61) \times 10^{-4}$	$(3.04 \pm 0.83) \times 10^2$
20000+3239	$(2.32 \pm 1.02) \times 10^{-5}$	$(2.79 \pm 0.81) \times 10^{-4}$	$(3.36 \pm 0.87) \times 10^3$	$(1.95 \pm 0.79) \times 10^{-4}$	$(1.23 \pm 0.44) \times 10^{-4}$	$(1.77 \pm 0.59) \times 10^2$
22223+4327	$(2.18 \pm 0.90) \times 10^{-5}$	$(4.93 \pm 1.36) \times 10^{-4}$	$(6.34 \pm 1.90) \times 10^3$	$(7.10 \pm 3.21) \times 10^{-4}$	$(4.12 \pm 1.57) \times 10^{-4}$	$(1.62 \pm 0.43) \times 10^2$
22272+5435	$(2.59 \pm 1.22) \times 10^{-5}$	$(3.75 \pm 1.23) \times 10^{-4}$	$(4.05 \pm 1.13) \times 10^3$	$(3.50 \pm 1.38) \times 10^{-4}$	$(1.70 \pm 0.56) \times 10^{-4}$	$(1.36 \pm 0.41) \times 10^2$
22574+6609	$(3.39 \pm 1.21) \times 10^{-4}$	$(1.72 \pm 0.50) \times 10^{-3}$	$(1.42 \pm 0.35) \times 10^3$	$(1.39 \pm 0.56) \times 10^{-3}$	$(2.81 \pm 0.91) \times 10^{-3}$	$(5.67 \pm 1.57) \times 10^2$
23304+6147	$(2.39 \pm 1.07) \times 10^{-5}$	$(3.45 \pm 1.21) \times 10^{-4}$	$(4.05 \pm 1.12) \times 10^3$	$(4.17 \pm 1.52) \times 10^{-4}$	$(4.87 \pm 1.51) \times 10^{-4}$	$(3.28 \pm 0.63) \times 10^2$

Table 6. Correlation Matrix among the 21 and 30 μm Features and the AGB and SW Mass Loss Rates
Derived from the PCA Multivariate Analysis

	F_{21}	F_{30}	\dot{M}_{AGB}/d^2	\dot{M}_{SW}/d^2
F_{21}	1.00	0.64	0.82	0.62
F_{30}	0.64	1.00	0.87	0.83
\dot{M}_{AGB}/d^2	0.82	0.87	1.00	0.80
\dot{M}_{SW}/d^2	0.62	0.83	0.80	1.00

Table 7. Comparison of the Mass Loss Rates (\dot{M}) Derived in This Work with That Reported in the Literature. All Are Based on the Same Distance and Gas-to-Dust Ratio as Those Adopted in This Work.

IRAS Sources	\dot{M} ($M_{\odot} \text{ yr}^{-1}$)	References	Methodology
Z02229+6208	AGB: 1.94×10^{-5} , SW: 5.53×10^{-4}	This work	IR SED
	1.4×10^{-4}	Hrivnak & Biegging (2005)	CO
	3.59×10^{-5}	Hrivnak et al. (2000)	IR SED
04296+3429	AGB: 3.84×10^{-5} , SW: 1.29×10^{-4}	This work	IR SED
	3.10×10^{-5}	Hrivnak & Biegging (2005)	CO
	1.75×10^{-5}	Sahai (1999)	Scattered Light
	6.30×10^{-6}	Bakker et al. (1997)	CN
	1.60×10^{-6}	Bakker et al. (1997)	C ₂
	4.00×10^{-5}	Bujarrabal et al. (2001)	CO
05113+1347	AGB: 2.59×10^{-5} , SW: 1.24×10^{-4}	This work	IR SED
	7.90×10^{-6}	Bakker et al. (1997)	CN
	7.90×10^{-7}	Bakker et al. (1997)	C ₂
	6.22×10^{-4}	Reddy & Parthasarathy (1996)	IRAS 60 μm Emission
	2.7×10^{-4}	Hrivnak et al. (2009)	IR SED
05341+0852	AGB: 1.01×10^{-5} , SW: 1.77×10^{-4}	This work	IR SED
	1.00×10^{-5}	Bakker et al. (1997)	CN
	1.00×10^{-6}	Bakker et al. (1997)	C ₂
	1.60×10^{-7}	Reddy & Parthasarathy (1996)	IRAS 60 μm Emission
	7.68×10^{-5}	Hrivnak et al. (2009)	IR SED
06530-0213	AGB: 1.86×10^{-5} , SW: 2.36×10^{-4}	This work	IR SED
	4.42×10^{-7}	Reddy & Parthasarathy (1996)	IRAS 60 μm Emission
	3.30×10^{-5}	Hrivnak & Biegging (2005)	CO
	7.71×10^{-5}	Hrivnak et al. (2009)	IR SED
07134+1005	AGB: 1.99×10^{-5} , SW: 1.24×10^{-4}	This work	IR SED
	9.7×10^{-6}	Omont et al. (1993)	CO
	1.2×10^{-4}	Hony et al. (2003)	IR SED
	5.1×10^{-6}	Meixner et al. (2004)	CO
	2.7×10^{-5}	Meixner et al. (2004)	IR SED
	2.3×10^{-5}	Hrivnak & Biegging (2005)	CO
	4.43×10^{-5}	Buemi et al. (2007)	IR SED
	1.47×10^{-5}	Hrivnak et al. (2000)	IR SED
	07430+1115	AGB: 5.78×10^{-5} , SW: 1.05×10^{-3}	This work
7.48×10^{-4}		Hrivnak et al. (2009)	IR SED
14429-4539	AGB: 3.22×10^{-5} , SW: 2.97×10^{-4}	This work	IR SED
	3.8×10^{-7}	Reddy & Parthasarathy (1996)	IRAS 60 μm Emission
16594-4656	AGB: 8.17×10^{-5} , SW: 7.98×10^{-4}	This work	IR SED
	1.27×10^{-4}	Hrivnak et al. (2000)	IR SED
19477+2401	AGB: 2.37×10^{-5} , SW: 1.44×10^{-3}	This work	IR SED
	1.52×10^{-4}	Hrivnak et al. (2000)	IR SED
19500-1709	AGB: 7.14×10^{-5} , SW: 4.34×10^{-4}	This work	IR SED
	8.97×10^{-5}	Clube & Gledhill (2004)	IR SED
	6.89×10^{-5}	Meixner et al. (1997)	IR SED
	2.02×10^{-5}	Likkel et al. (1991)	CO
	3.05×10^{-5}	Omont et al. (1993)	CO
20000+3239	AGB: 2.32×10^{-5} , SW: 1.95×10^{-3}	This work	IR SED
	3.47×10^{-5}	Buemi et al. (2007)	IR SED
	5.52×10^{-6}	Likkel et al. (1991)	CO
	1.16×10^{-5}	Hrivnak et al. (2000)	IR SED
	1.99×10^{-6}	Omont et al. (1993)	CO
22223+4327	AGB: 2.18×10^{-5} , SW: 7.10×10^{-4}	This work	IR SED
	6.14×10^{-6}	Likkel et al. (1991)	CO
	1.6×10^{-4}	Bakker et al. (1997)	CN
	2.5×10^{-5}	Bakker et al. (1997)	C ₂

Table 7—Continued

IRAS Sources	\dot{M} ($M_{\odot} \text{ yr}^{-1}$)	References	Methodology
22272+5435	AGB: 2.59×10^{-6} , SW: 3.50×10^{-4}	This work	IR SED
	1.88×10^{-5}	Bujarrabal et al. (2001)	CO
	4.2×10^{-5}	Buemi et al. (2007)	IR SED
	5.8×10^{-5}	Hrivnak & Bieging (2005)	CO
22574+6609	AGB: 3.39×10^{-5} , SW: 1.39×10^{-3}	This work	IR SED
	1.15×10^{-4}	Likkel et al. (1991)	CO
	1.36×10^{-4}	Hrivnak & Bieging (2005)	CO
	3.3×10^{-5}	Hrivnak et al. (2000)	IR SED
23304+6147	AGB: 2.39×10^{-5} , SW: 4.17×10^{-4}	This work	IR SED
	1.33×10^{-5}	Likkel et al. (1991)	CO
	1.4×10^{-5}	Hrivnak & Bieging (2005)	CO
	3.35×10^{-5}	Omont et al. (1993)	CO
	5.0×10^{-5}	Bakker et al. (1997)	CN
	1.0×10^{-5}	Bakker et al. (1997)	C ₂